

## Solar Tides as Revealed by Measurements of Mesosphere Temperature by the MLS Experiment on UARS

JEFFREY M. FORBES

*Department of Aerospace Engineering Sciences, University of Colorado, Boulder, Colorado*

DONG WU

*Jet Propulsion Laboratory, Pasadena, California*

(Manuscript received 29 March 2005, in final form 16 November 2005)

### ABSTRACT

Temperatures between 25 and 86 km measured by the Microwave Limb Sounder (MLS) experiment on the *Upper Atmosphere Research Satellite (UARS)* are analyzed to delineate diurnal, semidiurnal, and terdiurnal tidal structures and stationary planetary waves. These Fourier components are determined from temperatures averaged in bins covering 5° latitude, 30° longitude and 1 h in local time. This study confirms the presence of diurnal nonmigrating tides with zonal wavenumbers  $s = 0, 2, -3$  [ $s > 0$  ( $s < 0$ ) implying westward (eastward) propagation] and semidiurnal tides with  $s = 1$  and 3, and some components of lesser importance that were previously determined from UARS wind measurements near 95 km. The seasonal-latitude and height structures of these components are now revealed, and utilized to aid in interpreting their behaviors and ascertaining their origins. New discoveries include the terdiurnal  $s = 2$  and  $s = 4$  components, and trapped nonmigrating diurnal tides with  $s = 0$  and  $s = 2$ . The former are likely to arise from nonlinear interaction between the migrating ( $s = 3$ ) terdiurnal tide and the stationary planetary wave with  $s = 1$ . The latter may reflect the presence of a longitude-dependent in situ heat source, or in situ nonlinear interaction between the migrating diurnal tide and a stationary planetary wave with  $s = 1$ . The present results provide a rich mixture of observational results to challenge both mechanistic and general circulation models of the middle atmosphere. In addition, internal consistency is established between the MLS tidal temperatures at 86 km and previously derived tidal winds at 95 km within the context of tidal theory. This result represents one step in the validation of measurements required for successful application of data-model assimilation techniques to the mesosphere and lower thermosphere.

### 1. Introduction

The global temperature, density, and wind fields induced by the daily cyclic absorption of solar energy in an atmosphere are referred to as solar thermal tides. Assuming continuity in space and time around a latitude circle, solar thermal tidal fields are represented in the form

$$A_{n,s} \cos(n\Omega t + s\lambda - \phi_{n,s}), \quad (1)$$

where  $t$  = time (days),  $\Omega$  = rotation rate of the earth =  $2\pi \text{ day}^{-1}$ ,  $\lambda$  = longitude,  $n$  ( $= 1, 2, \dots$ ) denotes a sub-

harmonic of a solar day,  $s$  ( $= \dots -3, -2, \dots 0, 1, 2, \dots$ ) is the zonal wavenumber, and the amplitude  $A_{n,s}$  and phase  $\phi_{n,s}$  are functions of height and latitude. In this context,  $n = 1, 2, 3$  represent oscillations with periods corresponding to 24, 12, and 8 h, and hence are referred to as diurnal, semidiurnal, and terdiurnal tides, respectively. Eastward (westward) propagation corresponds to  $s < 0$  ( $s > 0$ ). The phase is defined as the time of maximum at zero longitude; in other words, the local time at Greenwich. (The alternative definition of longitude of maximum at  $t = 0$  is not used for tides, since the phase is undefined for  $s = 0$ .) At any height and latitude the total tidal response is obtained as a sum over  $n$  and  $s$ .

Rewriting (1) in terms of local time  $t_{LT} = t + \lambda/\Omega$ , we have

$$A_{n,s} \cos[n\Omega t_{LT} + (s - n)\lambda - \phi_{n,s}]. \quad (2)$$

---

*Corresponding author address:* Jeffrey M. Forbes, Dept. of Aerospace Engineering Sciences, University of Colorado, UCB 429, Boulder, CO 80305.  
E-mail: Forbes@colorado.edu

Solar radiation absorption by a zonally symmetric atmosphere or surface yields daily (local time) variations that are independent of longitude; that is,  $s = n$ . From (1) such components correspond to a zonal phase speed  $C_{\text{ph}} = d\lambda/dt = -n\Omega/s = -\Omega$ , in other words westward-propagating at the same speed as the apparent motion or migration of the sun to a ground-based observer. These sun-synchronous tidal components are referred to as migrating tides.

Now consider the cyclic heating due to absorption of solar energy by a zonally asymmetric (longitude dependent) planetary atmosphere or surface. In response to this heating, the local time structure of the atmosphere (at a given height and latitude) is dependent on longitude. A common approach is to examine zonal wavenumber components of the lowest-order local time harmonics (diurnal, semidiurnal, terdiurnal) that combine to give rise to the salient features of this longitude dependence. In this case, Fourier representation must involve a range of zonal wavenumbers of both sign, corresponding to waves propagating to the east ( $s < 0$ ) or west ( $s > 0$ ) (Chapman and Lindzen 1970). This approach offers the opportunity to relate results to tidal theory and numerical models, and often to gain physical insight. While some examples of longitudinally varying local time structures are illustrated in this paper, emphasis herein is focused on analysis and interpretation of the Fourier components of the temperature field.

Throughout the remainder of this paper we utilize the notation  $DW_m$  or  $DE_m$  to denote a westward- or eastward-propagating diurnal tide, respectively, with zonal wavenumber  $m = s$ . For semidiurnal and terdiurnal oscillations S and T replaces D. The standing oscillations are denoted D0, S0, T0, and stationary planetary waves (SPW) with zonal wavenumber  $m$  are expressed as  $SPW_m$ .

While nonmigrating tides were known to exist in surface pressure observations (Chapman and Lindzen 1970), their unambiguous identification in the mesosphere/lower thermosphere (MLT, ca. 60–120 km) was not possible until the advent of global satellite measurements at altitudes where the tidal signal is sufficiently large in comparison to other sources of variability (i.e., Lieberman 1991; Hagan et al. 1997b; Talaat and Lieberman 1999; Manson et al. 2002, 2004; Oberheide and Gusev 2002; Forbes et al. 2003). These studies were hampered by local time sampling limitations, thus severely affecting the altitude or latitude regime of the tidal determinations, the tidal period capable of being ascertained, or introducing aliasing uncertainties into the analyses. Nevertheless, the available observational analyses spawned a number of modeling investigations

seeking to explain the origins and characteristics of nonmigrating tides in the MLT (i.e., Ekanayake et al. 1997; Miyahara et al. 1999; Forbes et al. 2001; Hagan and Roble 2001; Grieger et al. 2002; Hagan and Forbes 2002, 2003). It is now generally accepted that nonmigrating tides in the upper atmosphere arise from at least two mechanisms: zonally asymmetric thermal forcing, and nonlinear interactions between tides and SPWs. For instance, it is well known that latent heating associated with deep tropical convection possesses strong variations with universal time (UT), longitude, latitude, and season. Studies by Hagan et al. (1997a), Forbes et al. (1997a, 2001), Hagan and Forbes (2002, 2003), and Oberheide et al. (2002) demonstrate that this source of excitation leads to diurnal and semidiurnal tides over a spectrum of zonal wavenumbers that propagate into the MLT and achieve significant amplitudes in this height regime.

Much evidence now exists that supports nonlinear wave-wave interactions as an important source of nonmigrating tides. The mechanism works as follows (Teitelbaum and Vial 1991). Given two oscillations with respective frequency-zonal wavenumber pairs  $(\sigma_1, s_1)$  and  $(\sigma_2, s_2)$ , and under the assumption of a so-called quadratic interaction between these two primary waves, and neglecting self-interactions, sum and difference secondary waves are generated with the frequency, zonal wavenumber pairs  $(\sigma_1 + \sigma_2, s_1 + s_2)$  and  $(\sigma_1 - \sigma_2, s_1 - s_2)$ . Teitelbaum and Vial (1991) invoked this mechanism as a secondary means (beyond direct solar heating) of exciting the migrating terdiurnal tide ( $n = 3, s = 3$ ), via interaction between the migrating diurnal ( $n = 1, s = 1$ ) and semidiurnal ( $n = 2, s = 2$ ) tides. These mechanisms for exciting the terdiurnal tide have recently been considered by Smith (2000) and Smith and Ortland (2001). Forbes et al. (1995) suggested nonlinear interaction between SW2 and SPW1 to explain the existence of a large SW1 tide over South Pole. Recent modeling work in fact indicates that nonlinear interactions between SPW1 and migrating tides lead to significant nonmigrating diurnal and semidiurnal tidal signatures above about 80-km altitude (Hagan and Roble 2001; Yamashita et al. 2002; Angelats i Coll and Forbes 2002; Lieberman et al. 2004; Grieger et al. 2004). There are of course many other combinations of tide-tide and tide-planetary wave interactions that may be effective in producing observable nonmigrating tidal signatures in the upper atmosphere. It is also arguable that the interaction of a zonally asymmetric distribution of gravity waves interacting with migrating tides could also generate nonmigrating tidal components (McLan-dress and Ward 1994).

One objective of the present work is to explore the

temperature measurements made by the Microwave Limb Sounder (MLS) instrument on the *Upper Atmosphere Research Satellite (UARS)* to establish the degree of longitude variability in the local time temperature structure, and to identify the primary nonmigrating tidal components responsible for the longitude variability. Similar analyses have been performed on wind measurements from *UARS* (Forbes et al. 2003; Huang and Reber 2004; Manson et al. 2004); however, these studies are restricted to 95 km and between  $\pm 42^\circ$  latitude where both day and night data were available to perform unambiguous separation between tidal components that could potentially alias into one another. Advantages of the MLS temperature measurements for this type of study include wider latitude coverage due to the nature of the instrumental sampling, and 24-h local time coverage over the  $\sim 25$ –86-km altitude range, thus allowing examination of vertical structures. The upper altitude limit of 86 km means, however, that the tidal amplitudes that we are seeking to identify have not yet achieved their altitude of maximum amplitude (around 110–150 km) and may be relatively small, thus admitting potential contamination from other temperature variations.

A second objective of this work is to explore the consistency between tidal winds at 95 km derived from the High-Resolution Doppler Imager (HRDI) and the Wind Imaging Interferometer (WINDII) instruments on *UARS* (Forbes et al. 2003), and the MLS tidal temperatures determined here at the altitude of 86 km. For reasons explained later, we focus on the Kelvin wave component of DE3 for this intercomparison, and utilize a technique (Svoboda et al. 2005) involving Hough mode extensions (Lindzen et al. 1977; Forbes and Hagan 1982) to perform the analysis. The outcome of this exercise is only one of many validation efforts that must be performed before data from multiple sources can be assimilated into models to specify the dynamical state of the MLT.

In the following section, the experimental data and method of analysis utilized to derive solar tides from the MLS temperatures are described. In section 3, we demonstrate the longitudinal variability of the observed temperatures in a local time frame, thus illustrating the aggregate effects of nonmigrating tides. Sections 4, 5, and 6 focus on the height, latitude, and monthly dependences of various zonal wavenumber components of the diurnal, semidiurnal, and terdiurnal tides, and inferences are made concerning potential sources for these waves. Section 7 is devoted to DE3, and use of the techniques noted above to examine consistency between winds and temperatures measured from *UARS*. Following a summary of results and conclusions, an ap-

pendix is provided to explain how the variability of stationary planetary waves can alias into the tidal signals that are the subject of this paper, and how bounds are estimated for this source of contamination for our derived tidal fields.

## 2. The experimental data and method of analysis

The data analyzed here consist of temperatures between 20 and 86 km derived from 63-GHz  $O_2$  emissions measured by the MLS on *UARS*. Descriptions of the experimental technique, instrument sampling, the retrieval algorithm and information on precision and validation are provided in Wu et al. (2003). The estimated precision of MLS temperatures varies from 1.5–4.0 K between 20 and 60 km, and 6.0–8.0 K between 60 and 85 km, and increases sharply above 90 km. Comparisons with other datasets suggest biases at some altitudes, but these are not expected to significantly affect the temperature variations described here.

Because the instrument views  $90^\circ$  to the satellite velocity vector in a 585 km and  $57^\circ$  inclination orbit, MLS latitude coverage on a given day extends from  $34^\circ$  in one hemisphere to  $80^\circ$  in the other. The satellite executes a  $180^\circ$  yaw maneuver 10 times a year, yielding alternative views of high latitudes every 36 days. The MLS experiment collected temperatures from September 1991–June 1997, with superior and near-continuous coverage during 1 November 1991–27 October 1994. The latter period is selected for the present analysis, due to its uniformity in longitude and UT sampling.

The temperature data were analyzed as follows to extract the tidal components, which represent 3-yr averages over the 1 November 1991–27 October 1994 period. Within each fitting interval (see below) temperatures were averaged in bins spanning  $24^\circ$  longitude,  $5^\circ$  latitude, and 1 h in UT at increments of 2-km altitude from 20 to 86 km. A standard deviation was computed for each hourly data point, primarily providing a measure of geophysical variability. At each altitude, latitude, and longitude, Fourier least squares fits were performed with respect to UT to determine amplitudes and phases of diurnal, semidiurnal and terdiurnal tidal components. One-sigma uncertainty estimates were computed for each frequency-component amplitude and phase, based upon the hourly standard deviations. The frequency components for all the longitudes were then subjected to fast Fourier transform (FFT) to perform the zonal wavenumber decompositions for  $s = -6$  to  $s = +6$ . Uncertainty estimates were computed for each zonal wavenumber component, taking into account the frequency-component uncertainties from the previous stage of analysis. Average temperatures in the longitude and UT bins were also subjected to a two-

dimensional FFT, determining the frequency and zonal wavenumber decompositions simultaneously, with little change in the results.

The above sampling and binning procedure must be set into the context of the constraints of instrument sampling imposed by the yaw cycle maneuvers. Figure 1 illustrates the spatial-temporal coverage for the MLS temperature data covering the complete 1 November 1991–27 October 1994 data interval; as such, it is slightly different than the yaw cycle coverage for any given year. Our time intervals for binning of data in local time are centered on the 15th of each month, and span 36 days at latitudes equatorward of  $\pm 34^\circ$ , and 72 days at higher latitudes. This ensures 24 h of local time coverage at most latitudes between  $\pm 80^\circ$  (for some months inadequate local time coverage occurred near the “yaw boundaries” at  $\pm 34^\circ$ ). At latitudes poleward of  $\pm 34^\circ$  the high-latitude sampling during many months (i.e., January, April, June, November in the Southern Hemisphere, and May, July, October, December in the Northern Hemisphere) consists of  $\sim 36$  continuous days such that they overlap most of the same month–days as the sampling equatorward of  $\pm 34^\circ$ . On the other hand, there are some months (i.e., February, March in the Southern Hemisphere, and August, September in the Northern Hemisphere) where the 36 days of high-latitude data coverage are continuous, but are centered near the beginning or end of an adjacent month (i.e., slipped  $\sim 18$  days from midmonth). There are also some months (i.e., May and December in the Southern Hemisphere, and November and January in the Northern Hemisphere), where the 15th of the month falls in the gap between yaw cycles, and about half the local times binned together originate in the previous and following yaw cycles. It is these latter months (in one hemisphere or the other) that may be most subject to aliasing of the type discussed in the appendix. However, the reader is reminded that the results described here are climatological in the sense that they represent multiyear averages. We have chosen to analyze the data in this fashion, rather than on a yaw cycle by yaw cycle basis, in order to obtain a data product that spans both hemispheres up to  $\pm 80^\circ$  without alternating data gaps between the yaw cycles. The multiyear averaging utilized here should ameliorate the shortcomings associated with this chosen methodology.

As is evident from Eq. (2), from sun-synchronous orbit ( $t_{LT} = \text{constant}$ ), all waves with the same value of  $(s - n)$  are indistinguishable from each other, in other words, they alias into each other. In the present context, this includes stationary planetary waves ( $n = 0, s = 1$ ), diurnal tides ( $n = 1$ ) with  $s = 0$  and  $s = 2$ ; semidiurnal tides ( $n = 2$ ) with  $s = 1$  and  $s = 3$ ; and terdiurnal tides

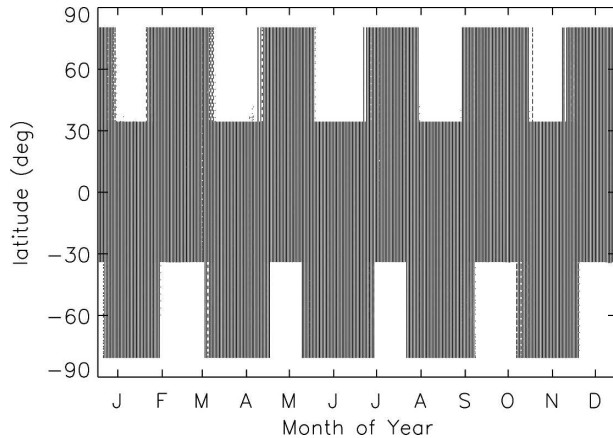


FIG. 1. MLS data coverage for the period 1 Nov 1991–27 Oct 1994.

( $n = 3$ ) with  $s = 2$  and  $s = 4$ . As satellite sampling precesses through local time, these aliasing effects are expected to decrease and ultimately disappear until all waves are fully sampled; that is all local times are sampled at all longitudes. In the present method, where we utilize 3-yr climatological averages filling all longitude and UT bins several times over at a given height and latitude, we expect our space–time decomposition to be alias-free from this point of view. (However, see below for aliasing effects due to nonstationarity of the dynamical fields.) Multiyear and monthly averaging also has the tendency to underestimate amplitudes when the dynamical fields exhibit year-to-year variability or nonstationarity during the fitting interval. It is difficult to assess the impact of these effects, but any future attempts at comparing model outputs with our results should address this problem through appropriate averaging of the model fields.

In at least two cases, nonstationarity of the dynamical fields can also lead to aliasing effects. For instance, as illustrated in the appendix, an SPW1 that evolves during the fitting interval can alias into all of the nonmigrating tidal components mentioned in the previous paragraph. A method for estimating potential aliasing contributions from this source is also provided in the appendix, and the resulting aliasing estimates are introduced throughout the following text and in the figure captions. In addition, as shown by Forbes et al. (1997b), a time-varying zonal mean field can alias into the migrating (sun-synchronous) tidal components, since from the satellite perspective it is not possible to distinguish between a true local time variation, and a zonal mean variation that projects onto the local-time precessing frame of the satellite. It is possible to greatly reduce this effect by taking (for *UARS*) a 36-day running mean through the data, subtracting this running mean from

the original data, and then analyzing the residuals to extract the tidal components (Forbes et al. 1997b). However, it is only possible to apply this method when the data are continuous in time (i.e., not subject to yaw maneuvers). For the present data, we applied this method equatorward of  $\pm 34^\circ$  latitude, and verified that nearly equivalent results were obtained for the binning method reported here. We suspect that the binning method (without removal of the running mean) may be more problematic when applied to a satellite that takes much longer than 36 days to precess in local time; for instance the 60-day precession period of the Thermosphere, Ionosphere, Mesosphere, Energetics and Dynamics satellite (*TIMED*).

### 3. Local time structures

Given that the present study focuses on solar thermal tides, it is natural to first examine the temperature structures revealed by the MLS experiment ordered in local time. Figure 2 provides plots of hourly temperatures at 86 km versus local time, at  $0^\circ$  and  $-60^\circ$  latitude and at six longitudes between  $12^\circ$  and  $300^\circ\text{E}$  for the month of March. These data are typical of other months as well. Each point corresponds to a 1-h average as described in section 1, and the vertical lines represent  $1\sigma$  standard deviations about the mean values in each local time bin. This figure also offers an opportunity to provide a measure of the geophysical variability in the data, as manifested in the displayed standard deviations. The thick solid lines in Fig. 2 represent least squares fits corresponding to superposition of diurnal, semidiurnal, and terdiurnal Fourier harmonics. It is readily apparent that the local time structures as well as mean values vary significantly with longitude; the former implies the existence of nonmigrating tides, the latter with stationary planetary waves. The changes in local time structure with longitude imply the presence of diurnal, semidiurnal, and perhaps terdiurnal nonmigrating tides, as discussed in connection with Eq. (2). The following sections primarily focus on the depiction of these tidal components and their interpretation.

### 4. Spectral overview

As noted previously, at a given longitude the local time structure is reasonably approximated by a superposition of diurnal, semidiurnal, and terdiurnal harmonics [i.e.,  $n = 1, 2, 3$  in Eq. (2)]. The variation with longitude of the local time structure is embodied in a spectrum of zonal wavenumbers [i.e.,  $s$  values in Eq. (2)] for each  $n$ th harmonic. In theory an infinite sum is required to capture the longitude variation of each harmonic, but in practice relatively few harmonics are

found to dominate. This point is illustrated in Fig. 3, wherein power spectra (i.e., square of temperature amplitude) are illustrated for stationary planetary waves, and the diurnal and semidiurnal nonmigrating tidal components, for July and January at 86 km. Migrating tides are omitted from this figure in order to highlight the smaller-amplitude nonmigrating components. We note that results in Fig. 3 at latitudes  $< -40^\circ$  for D0 and DW2 during July, and  $> +40^\circ$  for SW1 during January, may contain significant aliasing contributions due to SPW1 variability (see the appendix).

Figure 3 provides insight into potential sources for the observed nonmigrating tides. For instance, it is now generally accepted (i.e., Conrath 1976; Zurek 1976; Tokioka and Yagai 1987; Yagai 1989; Hendon and Woodberry 1993; Williams and Avery 1996; Forbes et al. 2001) that to first-order zonal asymmetries in surface or atmospheric properties characterized by zonal wavenumber  $m$  modulate absorption of the  $n$ th harmonic of diurnally varying solar radiation to excite the sum and difference thermal tides with frequency  $n\Omega$  and zonal wavenumbers  $n \pm m$ . Existence of DW2 and D0 in Fig. 3 is thus consistent with nonlinear interaction between DW1 and SPW1 (Hagan and Roble 2001) although these components can also be excited by latent heating in the troposphere, wherein a similar interaction between the DW1 component of solar radiation and the  $s = 1$  component of topography/land-sea contrast exists (Hagan and Forbes 2002). Similar interactions between SW2 (TW3) with SPW1 or  $s = 1$  topography, lead to SW1 and SW3 (TW2 and TW4) tidal components that also figure prominently in the power spectrum of Fig. 3. The SE2 and SW6 pair in July are consistent with modulation of SW2 radiation absorption by the  $m = 4$  component of topography/land-sea contrast, which is dominant at low latitudes (Yagai 1989). These semidiurnal nonmigrating tides were found by Manson et al. (2004) to be among the most important semidiurnal nonmigrating tides from their analysis of the UARS/HRDI wind measurements. Most likely, the DE2 and DE3 components evident in Fig. 3 are directly forced in the troposphere by latent heating (Forbes et al. 2001). These tidal components have significantly longer vertical wavelengths than their westward-propagating counterparts, are thus less susceptible to dissipation, and hence more likely to penetrate to the MLT (Ekanayake et al. 1997).

Figure 4 provides a height versus month perspective on the amplitude structures of SPW1, D0, DW1, and DW2 at  $-60^\circ$  latitude. The maximum in DW1 between 40 and 60 km is probably an in situ response to UV absorption by ozone, whereas the elevated amplitudes above 80 km may be due to the absorption of shorter-

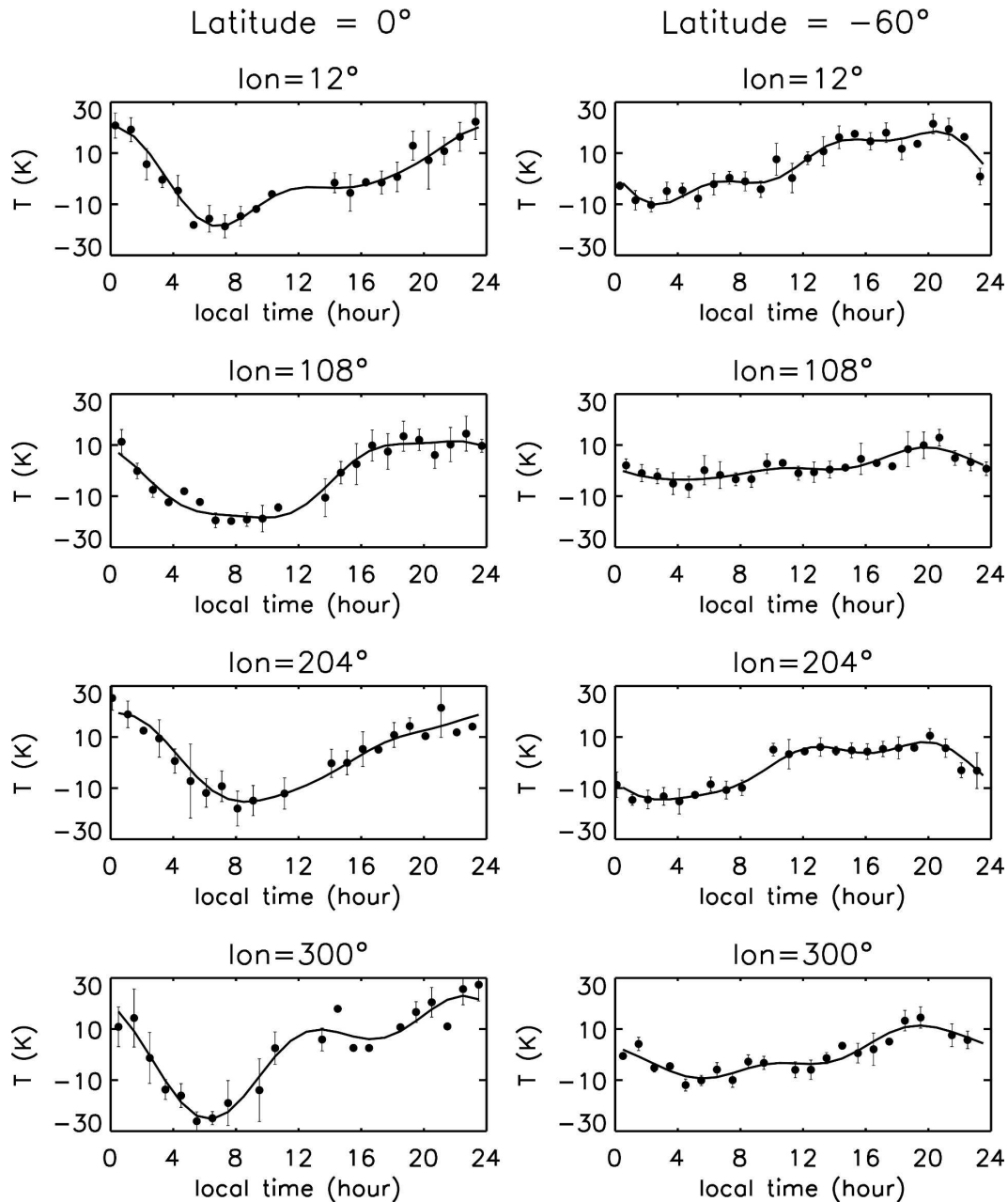


FIG. 2. Temperature differences from the zonal mean in March at 86 km for longitudes (top to bottom) 12°, 108°, 204°, and 300°, for latitudes (left) 0° and (right) -60°. The points represent hourly means over 1 Nov 1991–27 Oct 1994 for the 5° latitude × 24° longitude bins centered on the given latitudes and longitudes, and the vertical bars represent one standard deviation about the mean value.

wavelength UV radiation by O<sub>2</sub>, perhaps augmented by an effect of electrodynamic origin penetrating downward from the auroral ionosphere. The origin of the peak amplitudes near 70 km is unknown, but may be a signature of chemical heating (Mlynczak and Solomon 1993; Smith et al. 2003).

While SPW1 exhibits maximum values in Fig. 4 during late winter, the amplitude of DW2 is virtually nil

below 60 km, and only ~1.0 K below 50 km for D0. In the latter case it is reasonable to argue that some of the upper-level (>50 km) response is due to zonally symmetric tides propagating upward from a nonlinear interaction region below, since according to classical tidal theory the D0 temperature response is nonzero in the polar regions for the fundamental propagating mode (see Fig. 6). However, for DW2 any response at -60°

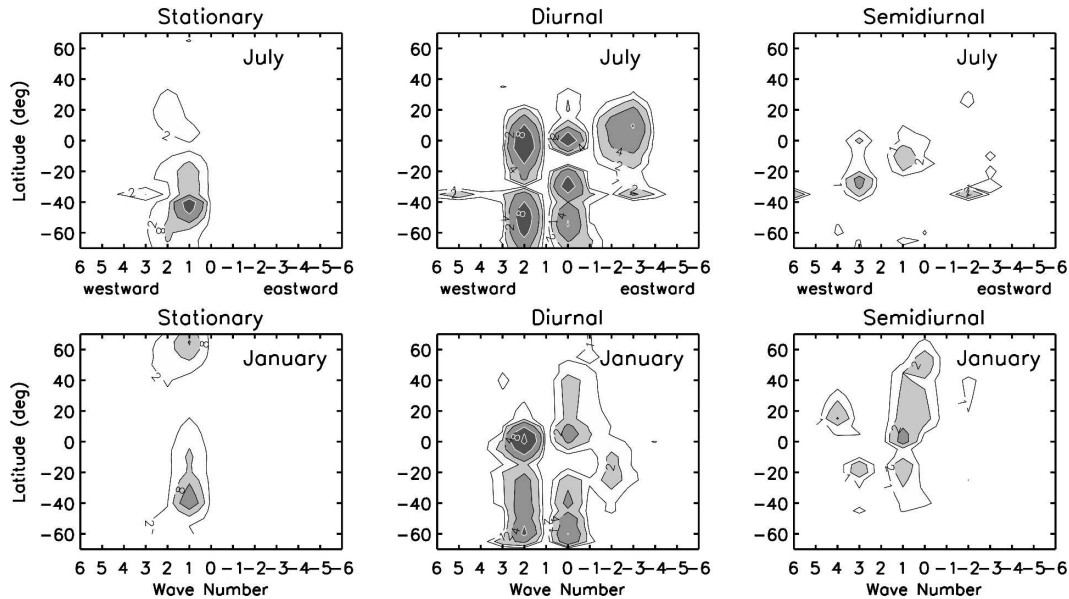


FIG. 3. Power spectra for temperature ( $K^2$ ) at 86 km for (left) stationary, (middle) diurnal, and (right) semidiurnal components as a function of latitude and zonal wavenumber (positive westward) for (top) July and (bottom) January. The migrating tidal components are excluded in order to more clearly illustrate the nonmigrating components. Interpolation was performed during January near  $\pm 34^\circ$  due to missing data points. As demonstrated in the appendix, results at latitudes  $< -40^\circ$  for D0 and DW2 during July, and  $> +40^\circ$  for SW1 during January, may contain significant aliasing contributions due to SPW1 variability.

latitude must occur in connection with trapped components, and hence an in situ source of excitation. The lack of similarity between the SPW1, D0, and DW2 amplitudes over the whole domain is consistent with the absence of the type of aliasing addressed in the appendix. Note also that the diurnal nonmigrating tides tend to show their largest amplitudes where signatures of both DW1 and SPW1 are relatively large, possibly reflecting the nonlinear generation of nonmigrating tides in these regions. We note in this context that upper bounds on aliasing contributions to D0 and DW2 due to SPW1 variability are estimated to be no more than 12% of the illustrated SPW1 amplitudes (see the appendix).

The counterpart of Fig. 4 for the semidiurnal tide is provided in Fig. 5, where height versus month contours of temperature amplitude are depicted for SPW1, SW2, SW1, and SW3 at  $+60^\circ$  latitude. Note that SW2 amplitudes are of order 2.0–4.0 K above 70 km during all months except December and January, and between 25 and 70 km during most months except for May, June, and July. SPW1 amplitudes are of order 4–10 K between 20 and 85 km, confined mainly to October through April. Based on these results, one would expect the nonlinear generation of the sum and difference waves SW1 and SW3 to be confined to the height versus month regime of significant SPW1 and SW2 ampli-

tudes. Distributions of the SW1 and SW3 amplitudes are broadly consistent with this. However, the alternate possibility of aliasing due to time evolution of the SPW1 amplitudes during the fitting intervals must be considered. According to our estimates in the Appendix, if the amplitudes of SW1 and SW3 below 50 km solely represent aliasing contributions due to SPW1 variability, then aliasing contributions at all altitudes may be as large as 33% of SPW1 amplitudes. Considering this possibility, the following depictions of nonmigrating tides are confined to 86 km, where the amplitudes are generally largest and the aliasing effects due to SPW1 are minimized.

## 5. Hough components

It is sometimes illustrative to examine tidal structures in terms of Hough functions, the eigenfunctions of Laplace's tidal equation (Chapman and Lindzen 1970). In particular, for the diurnal tide, which consists of both propagating and trapped components, some insight into the possible existence of in situ excitation may be revealed. In addition, the relative importance of various Hough functions for propagating components can also provide some insight into vertical structures by virtue of the connection between eigenfunctions, eigenvalues, and vertical wavelenghts (Chapman and Lindzen 1970).

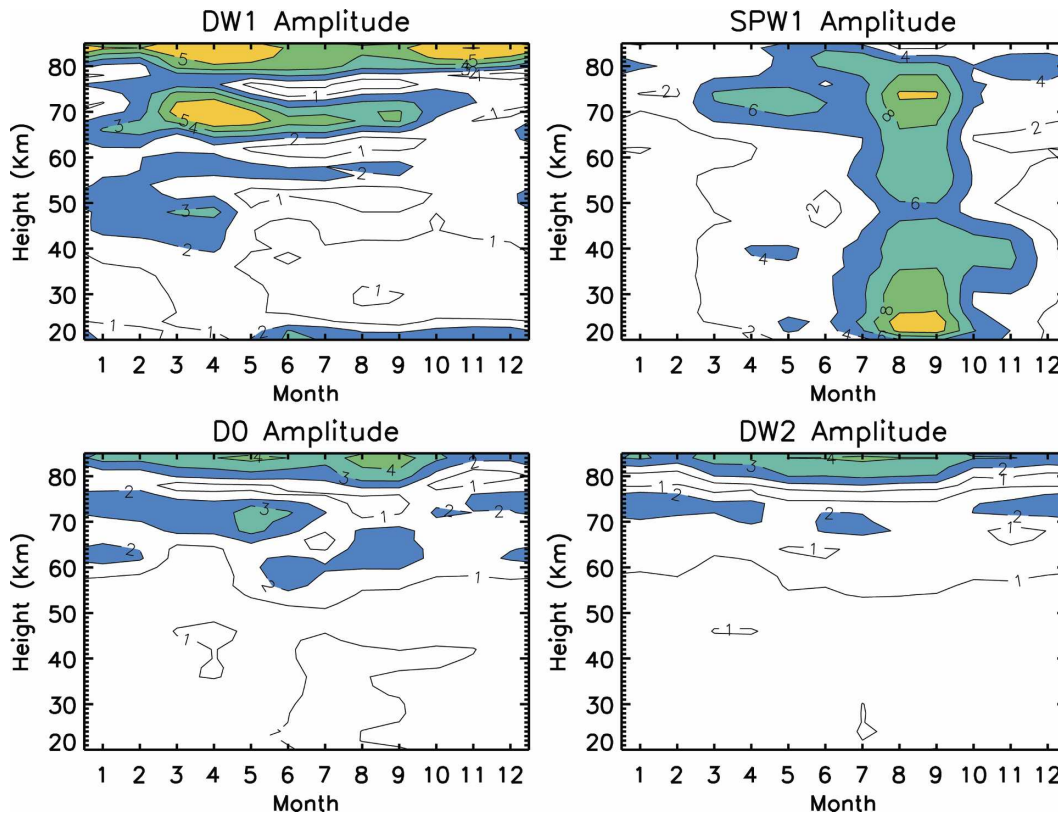


FIG. 4. Temperature amplitudes (K) for (top left) DW1, (top right) SPW1, (bottom left) D0, and (bottom right) DW2 as a function of height and month at  $-60^\circ$  latitude. Contour spacing is 1 K for tidal components and 2 K for SPW1. Aliasing contributions due to SPW1 variability (see the appendix) may be contained in the illustrated D0 and DW2 amplitudes. Upper bounds on these contributions are roughly 12% of the illustrated SPW1 amplitudes.

Hough functions for the diurnal tides with zonal wavenumbers  $s = 0$ ,  $s = 1$ ,  $s = 2$ , and  $s = -3$  are provided in Fig. 6. For each wavenumber, Hough functions for the first symmetric and antisymmetric propagating (index  $m$  positive in Fig. 6) and trapped (index  $m$  negative) modes are displayed. In contrast to the other wavenumbers, note that for  $s = 0$ : (i) the first propagating mode is antisymmetric while the first trapped mode is symmetric, (ii)  $s = 0$  modes can be nonzero at the poles, and (iii) the trapped modes maximize at the poles. Note also the well-known characteristics of diurnal Hough functions: the propagating components maximize at low latitudes ( $<30^\circ$ ), whereas the trapped modes maximize at middle to high latitudes.

Figure 7 illustrates the amplitudes and phases of D0, DW1, and DW2 at 86 km (solid points with  $1\sigma$  standard deviations), along with fits (solid lines) obtained by reconstruction using the first two propagating and first two trapped Hough modes for each zonal wavenumber. In this depiction aliasing contributions to D0 and DW2 amplitudes due to SPW1 variability (see the appendix) are estimated to be no more than 0.4 K. The D0 am-

plitudes are characterized by relatively high  $\sigma$  values, and no further interpretation will be attempted, although the coherence between independently derived phases at different latitudes may be worthy of note. DW1 amplitudes maximize at about 9 K near the equator, reflecting dominance of the first symmetric propagating component of the diurnal oscillation. However, the broadness of this structure and to some degree the nonsymmetric phase structure suggests the presence of higher-order modes. (Of course, much better agreement could be obtained by adding more Hough modes, as these functions form a complete orthogonal set.) The DW2 amplitudes are reasonably represented by the first four Hough modes. Examination of the Hough mode amplitudes reveals that the most important contributions to DW1 and DW2 are the first symmetric propagating modes, but that the trapped modes also make important contributions, as might be expected from the measured amplitudes at middle to high latitudes. This implies that part of the excitation lies at lower altitudes (see the introduction), but that there is an in situ excitation mechanism for generating evanes-

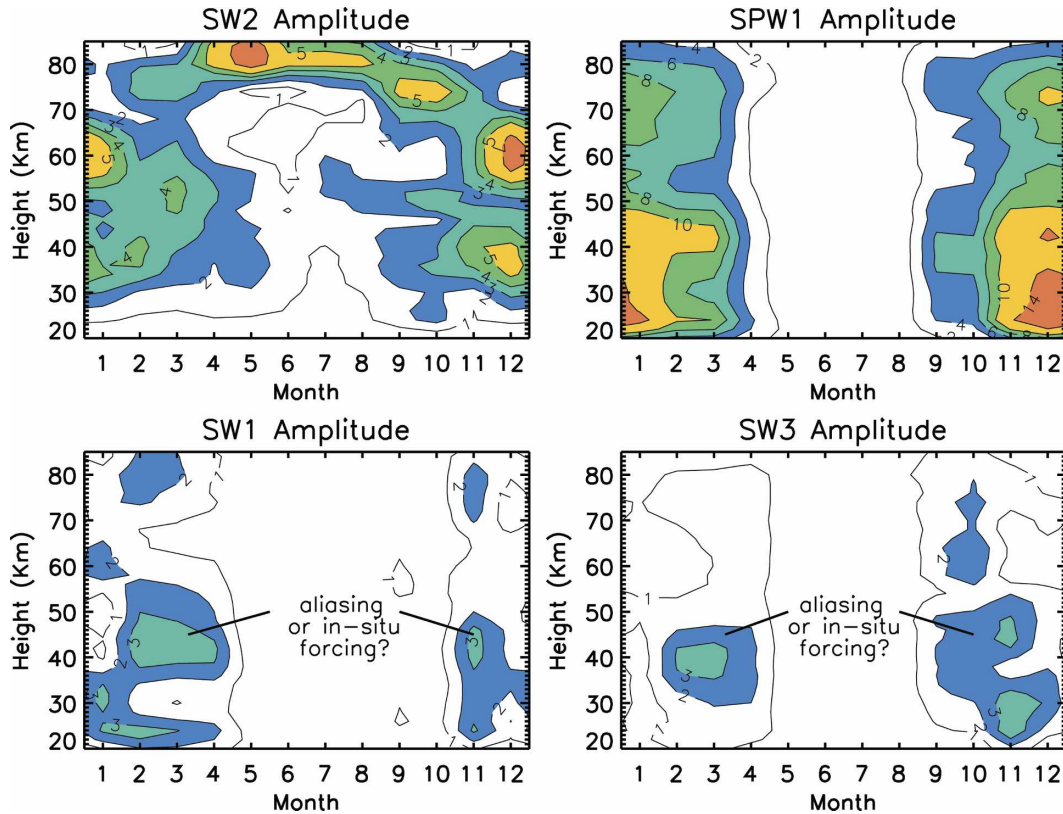


FIG. 5. Temperature amplitudes for (top left) SW2, (top right) SPW1, (bottom left) SW1, and (bottom right) SW3 as a function of height and month at  $+60^\circ$  latitude. Contour spacing is 1 K for tidal components and 2 K for SPW1. If the amplitudes of SW1 and SW3 below 50 km solely represent aliasing contributions to SPW1 variability (see the appendix), then aliasing contributions at all altitudes may be as large as 33% of SPW1 amplitudes (i.e.,  $\leq 1.3$  K at 86 km between November and February). However, it is possible that these amplitudes may represent, in whole or in part, signatures of nonlinear interaction between SW2 and SPW1, which would reduce this aliasing estimate accordingly.

cent or trapped tidal components as well. One possibility might be broadening (i.e., mode coupling) due to dissipation in this height regime (Lindzen and Hong 1974; Lindzen et al. 1977; Forbes and Hagan 1982). Another possibility is an in situ heat source, possibly chemical heating (Mlynczak and Solomon 1993; Smith et al. 2003), which would likely only directly excite the migrating (sun-synchronous) tide. The corresponding trapped components for D0 and DW2 could in principle result from in situ nonlinear interaction between DW1 and SPW1. In principle, of course, D0 and DW2 could result from a longitude-dependent heat source as well, but there is no known evidence for expecting significant zonal asymmetries in the background atmospheric state at these altitudes.

Also included in Fig. 7 (dashed lines) are values from the Global-Scale Wave Model (GSWM; Hagan and Forbes 2002). For D0 and DW2, the GSWM only includes excitation due to latent heating in the tropical troposphere, whereas for DW1 forcing due to insola-

tion absorption by  $\text{H}_2\text{O}$ ,  $\text{O}_3$ , and  $\text{O}_2$  in the troposphere, stratosphere, and mesosphere, respectively, are also accounted for (Hagan et al. 1999). The GSWM reasonably approximates the DW1 observations at low latitudes, albeit shifted about  $10^\circ$  northward, and with a few hours difference in phase. However, at higher latitudes the GSWM significantly underestimates the observed temperature amplitudes of all three tidal components in Fig. 7, especially in the Southern Hemisphere. This may imply omission of an in situ heat source of unknown origin in the GSWM. The GSWM significantly underestimates amplitudes for D0 and DW2 at low latitudes as well, suggesting that latent heat release is unimportant for exciting these oscillations, and that nonlinear interaction between DW1 and SPW1 is the dominant forcing mechanism (Hagan and Roble 2001; Lieberman et al. 2004; Grieger et al. 2004).

Figure 8 provides a similar illustration for the zonal wavenumber  $s = 1, 2,$  and  $3$  semidiurnal tides for January at 86 km. Aliasing contributions due to SPW1 vari-

### Diurnal Hough Functions

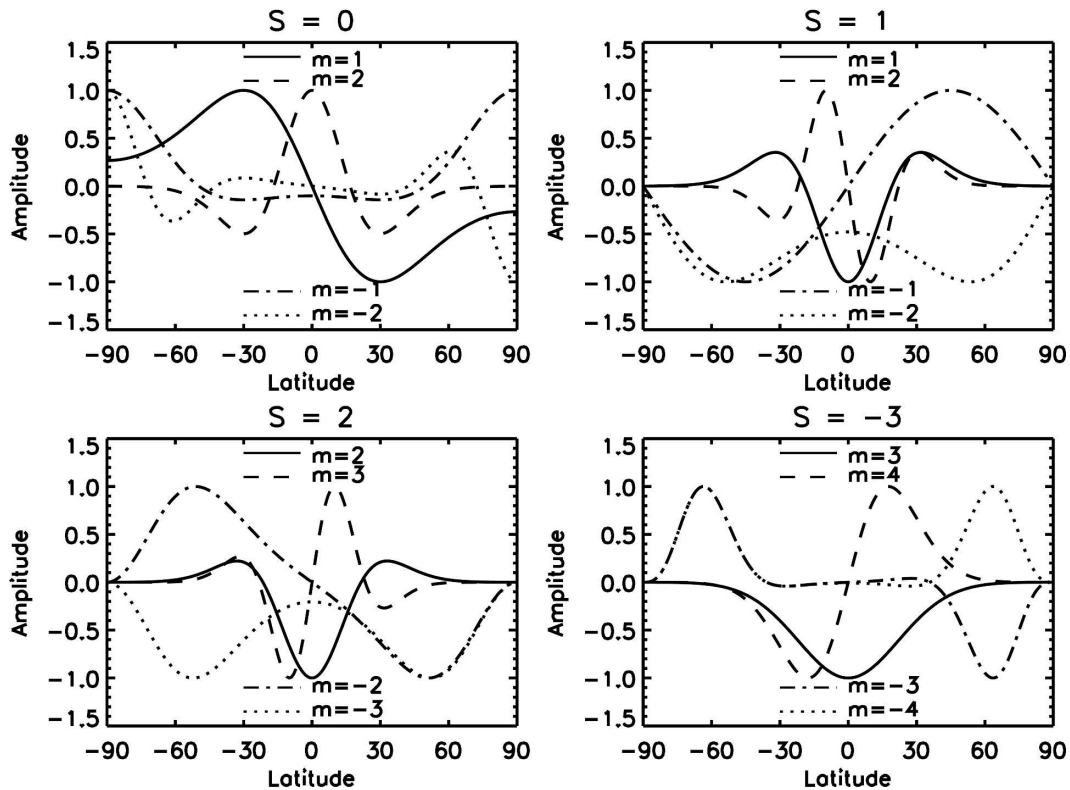


FIG. 6. Diurnal Hough functions for zonal wavenumbers  $s = 0$  (D0),  $s = 1$  (DW1),  $s = 2$  (DW2), and  $s = -3$  (DE3). The index  $m$  is related to the number of nodes in latitude, and is positive for propagating modes and negative for trapped modes.

ability (see the appendix) are estimated to be no more than 0.2 K for SW3, and less than 0.4 K at nearly all latitudes for SW1. For the semidiurnal tide, and the terdiurnal tidal component that will be discussed momentarily, we have only fit the first symmetric and first antisymmetric Hough modes to the data, as reasonable global fits can be accomplished this way, and differences between the observations and fits provide a measure of the importance of higher-order modes. The sun-synchronous ( $s = 2$ ) semidiurnal tide maximizes near 6 K at  $-10^\circ$  latitude, and reflects significant differences between the 2-mode Hough reconstruction and the measurements at latitudes poleward of about  $\pm 30^\circ$  latitude. This is not surprising, as the (2, 4), (2, 5), and even (2, 6) Hough modes have often been cited as contributing to global semidiurnal tidal wind structures (Lindzen 1976; Forbes et al. 1994; Forbes 1982; Forbes and Vial 1989, 1991). On the other hand, the SW1 and SW3 amplitude and phase structures are represented well by the first symmetric and antisymmetric Hough modes. The amplitudes of these nonmigrating tidal components maximize near 2.0 K, and depending on

the latitude each attains values of order 30%–50% of the migrating component.

Estimates of SW1, SW2, and SW3 from the GSWM (Hagan and Forbes 2003; Hagan et al. 1999) are also illustrated in Fig. 8 (dashed lines). For SW1 and SW3, the only tidal forcing in the GSWM is that associated with latent heating due to deep tropical convection, whereas all known forcing mechanisms are included for SW2 (Hagan et al. 1999). The model reproduces the observed phases of SW2 extremely well, but there are major model-data differences in amplitude southward of  $+10^\circ$  latitude. These differences are likely associated with inadequate treatment of mode coupling in the model (i.e., the generation of high-order modes) due to interaction of the migrating semidiurnal tide with the zonal mean wind field. For SW1 and SW3, the model values significantly underestimate the observations, suggesting that the primary forcing mechanism for these oscillations is nonlinear interaction between SW2 and SPW1 (Teitelbaum and Vial 1991; Forbes et al. 1995; Yamashita et al. 2002; Angelats i Coll and Forbes 2002; Grieger et al. 2004).

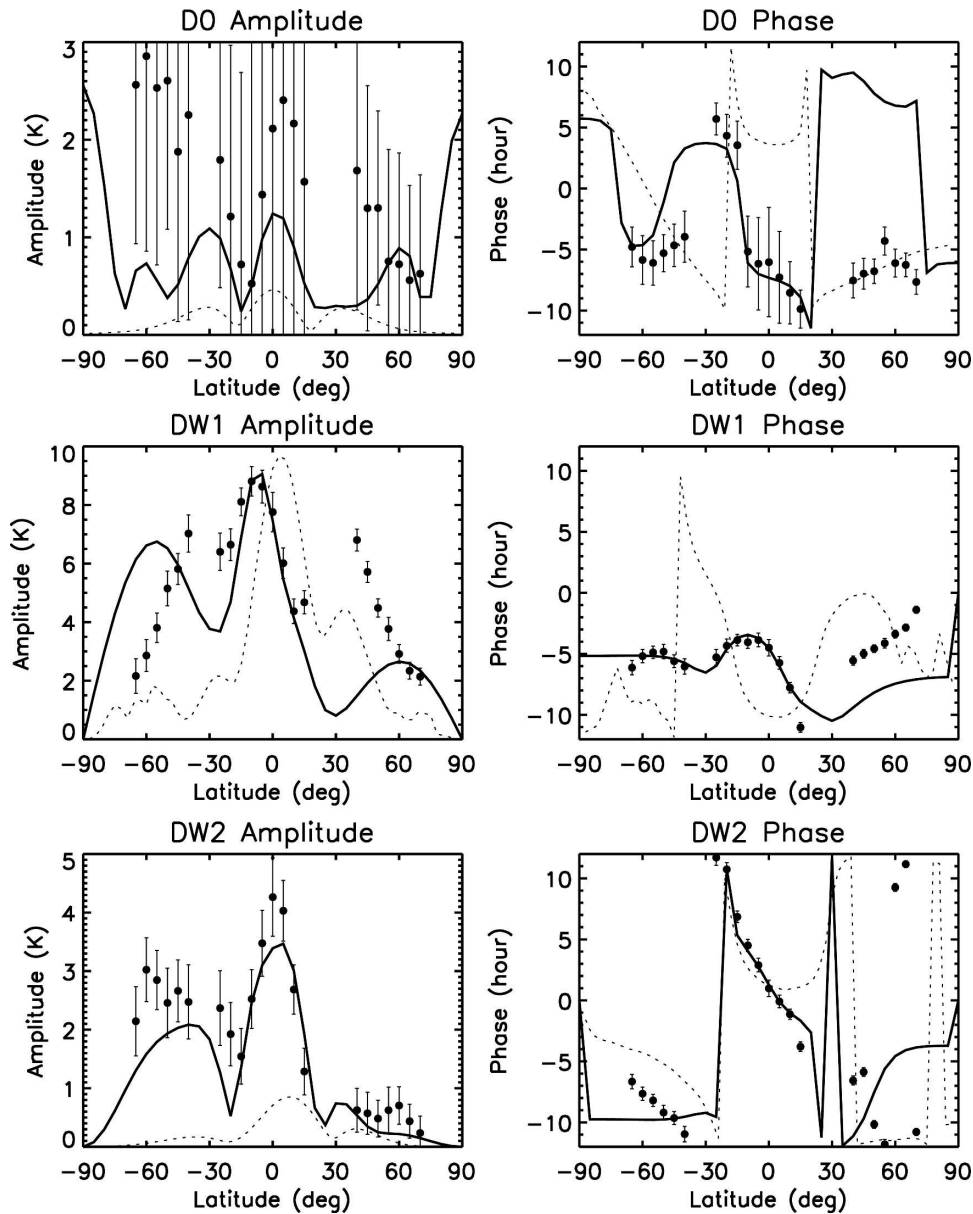


FIG. 7. Latitude structures of January diurnal (left) temperature amplitude and (right) phase at 86 km altitude for (top) D0, (middle) DW1, and (bottom) DW2. The solid lines represent Hough mode fits to these data taking into account the first two symmetric and antisymmetric propagating and trapped modes. The vertical bars represent  $1\sigma$  uncertainty estimates from the least squares fitting algorithm, calculated from standard deviations like those plotted in Fig. 2. The dashed lines are values from the GSWM taking into account forcing only by latent heat release in the Tropics (Hagan and Forbes 2002) for D0 and DW2; model results for DW1 contain all known sources of excitation (Hagan et al. 1999). Aliasing contributions to D0 and DW2 amplitudes due to SPW1 variability (see the appendix) are estimated to be no more than 0.4 K.

The corresponding depiction for the terdiurnal tides is provided in Fig. 9. Here the amplitudes are smaller, of order 0.5–2.0 K, and subject to larger variability and relative errors. However, aliasing contributions to TW2 and TW4 amplitudes due to SPW1 variability (see the

appendix) are estimated to be less than 0.2 K. Some degree of coherence in phases between latitudes (and altitudes, not shown) lends some credibility to the existence of these structures as independent propagating oscillations. These oscillations are not important to the

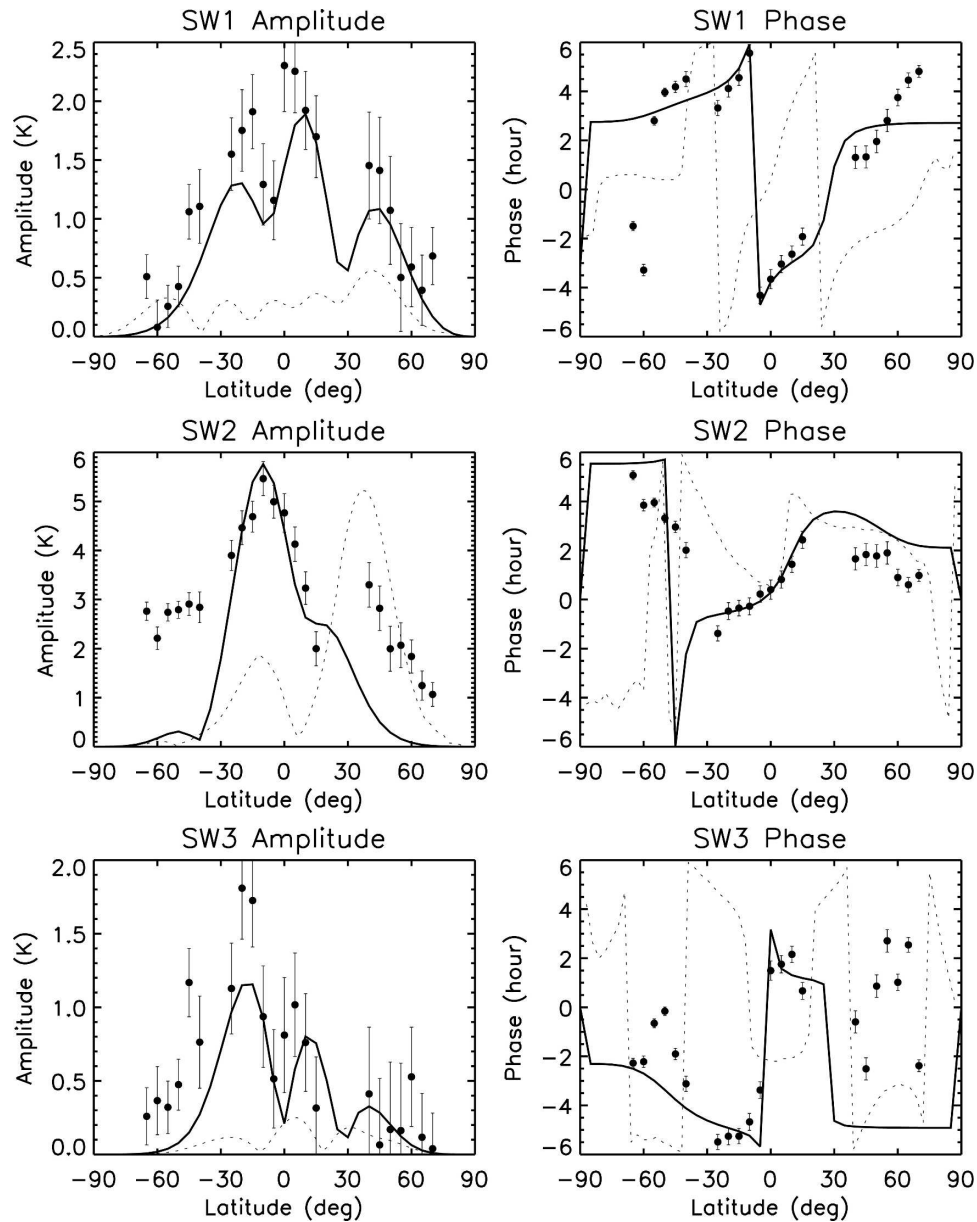


FIG. 8. Same as Fig. 7, except for SW1, SW2, and SW3. The dashed lines are values from the GSWM taking into account forcing only by latent heat release in the Tropics (Hagan and Forbes 2003) for SW1 and SW3; model results for SW2 contain all known sources of excitation (Hagan et al. 1999). Aliasing contributions due to SPW1 variability (see the appendix) are estimated to be no more than 0.2 K for SW3, and less than 0.4 K at nearly all latitudes for SW1.

dynamics of the upper mesosphere. However, due to their long vertical wavelengths, they can be expected to achieve significant amplitudes in the 120–170-km region and above, and possibly contribute to the dynamo generation of electric fields and other aspects of the variability of the region. Since experimental data for the atmosphere above 100 km is particularly sparse, efforts like the present one, supplemented by tidal models or GCMs with lower boundaries in the mesosphere, can

provide some insight into dynamical consequences at upper levels. In addition, the existence of nonmigrating tidal oscillations can provide clues to nonlinear interactions that may be occurring at lower levels of the atmosphere.

### 6. Seasonal–latitudinal structures

A perspective on seasonal–latitudinal variability of the diurnal tidal oscillations is provided in Fig. 10. Lati-

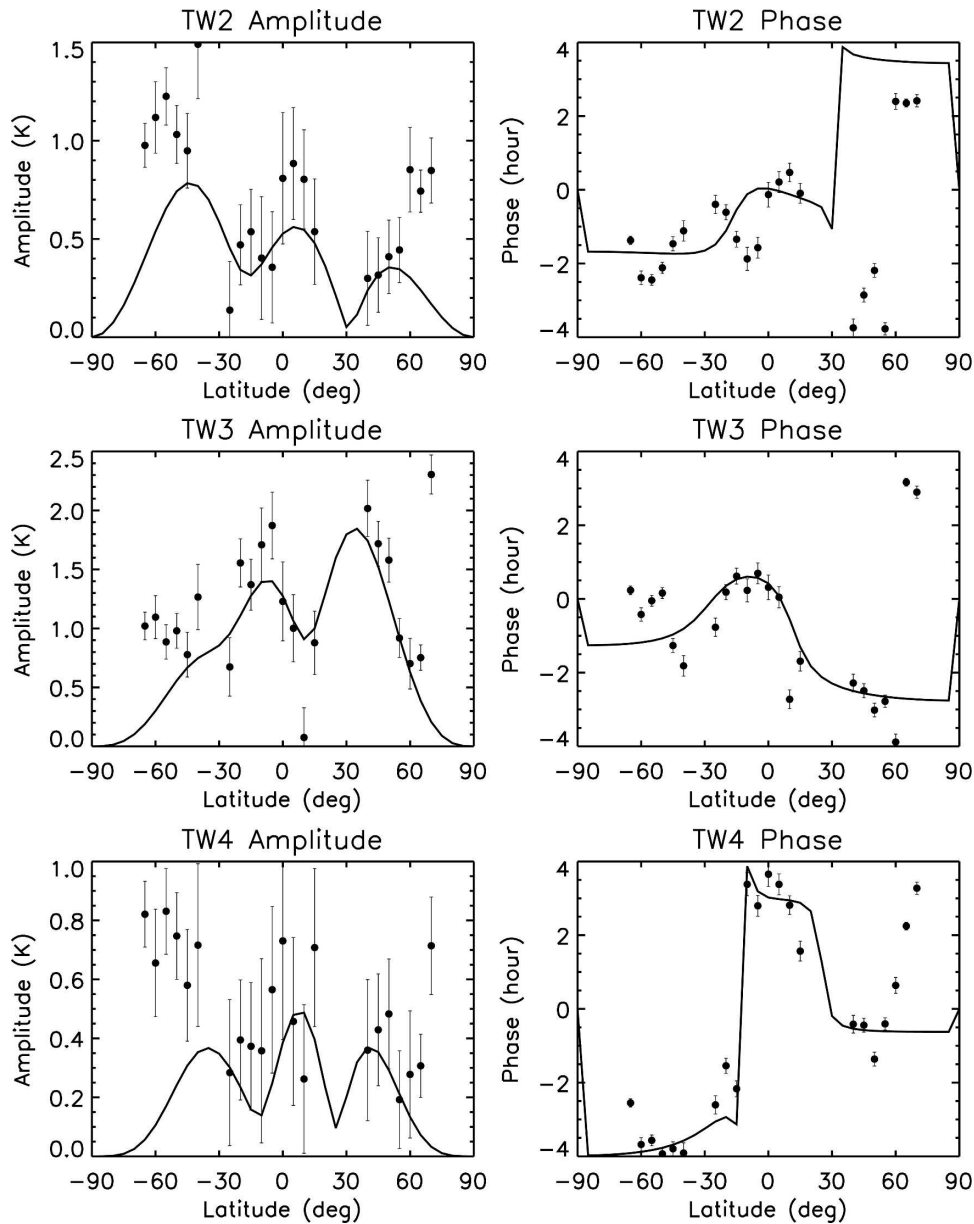


FIG. 9. Same as Fig. 7, except for TW2, TW3, and TW4. Terdiurnal results from the GSWM do not currently exist. Aliasing contributions to TW2 and TW4 amplitudes due to SPW1 variability (see the appendix) are estimated to be less than 0.2 K.

tude versus month contours of diurnal temperature amplitudes at 86-km altitude for D0, DW1, and DW2 are depicted. Upper bounds on aliasing contributions to D0 and DW2 amplitudes due to SPW1 variability (see the appendix) are estimated to be no more than 0.5 and 0.24 K, respectively, poleward of  $\pm 40^\circ$  latitude during local winter, and about half these values during local summer, and equatorward of these limits during all months of the year. These estimates are based upon an average SPW1 amplitude of 4.0 K at high latitudes dur-

ing local winter, and about 2.0 K at other times and locations. Amplitudes for DW1 are of order 4–10 K, while that of D0 and DW2 are of order 1–4 K. DW1 exhibits maxima within the  $\pm 40^\circ$  latitude regime that are primarily associated with propagating components, but significant amplitudes also exist at higher latitudes that reflect the presence of trapped components. Similar features are found in the amplitudes of D0 and DW2, but curiously, the high-latitude maxima are confined to the Southern Hemisphere and show relatively

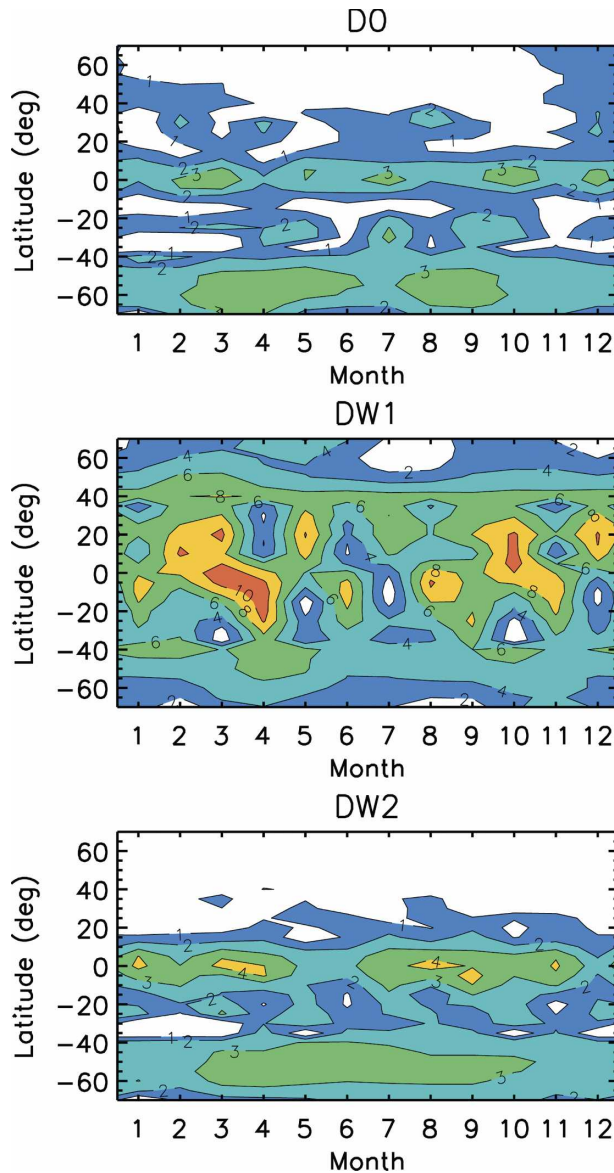


FIG. 10. Latitude vs month contours of D0, DW1, and DW2 diurnal temperature amplitudes at 86 km. Contour spacing is 1 K for D0 and DW2, and 2 K for DW1. Upper bounds on aliasing contributions to D0 and DW2 amplitudes due to SPW1 variability (see the appendix) are estimated to be no more than 0.5 and 0.24 K, respectively, poleward of  $\pm 40^\circ$  latitude during local winter, and about half these values during local summer, and equatorward of these limits during all months of the year. These estimates are based upon an average SPW1 amplitude of 4.0 K at high latitudes during local winter, and about 2.0 K at other times and locations.

little dependence on time of year. The diurnal tidal wind amplitudes for D0 at 95 km, as displayed in Forbes et al. (2003), also exhibit this same asymmetry between hemispheres, but their results only extend to  $\pm 42^\circ$  latitude. The origin of this latitudinal asymmetry remains

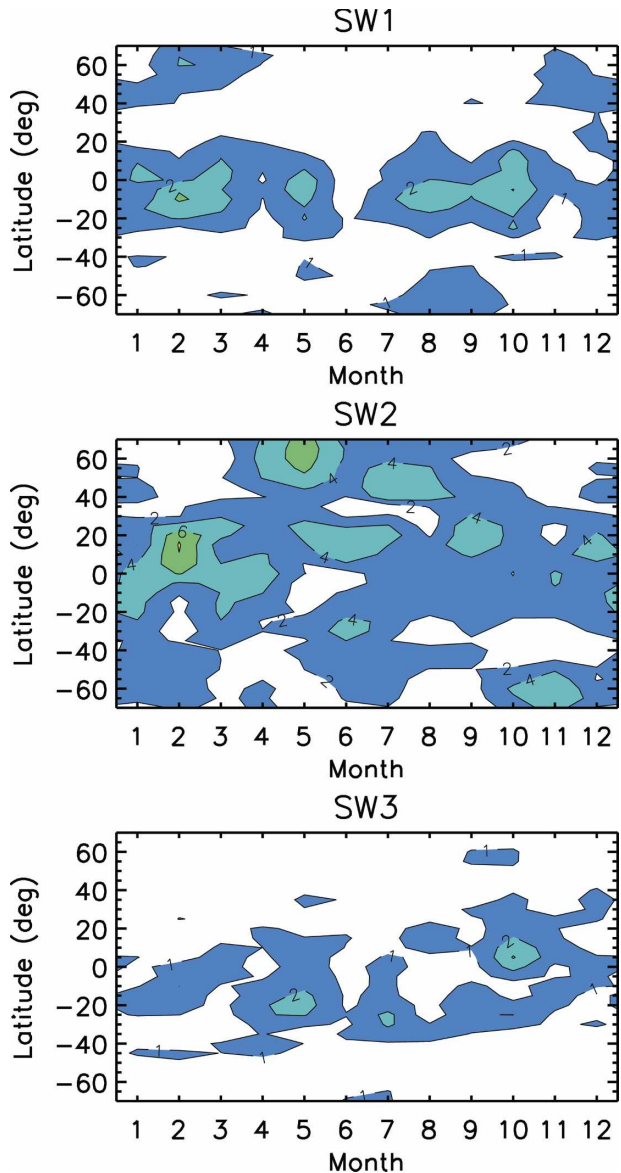


FIG. 11. Same as Fig. 10, except for SW1, SW2, and SW3. Contour spacing is 1 K for SW1 and SW3, and 2 K for SW2. Upper bounds on aliasing contributions to SW1 and SW3 amplitudes due to SPW1 variability (see the appendix) are estimated to be no more than 1.2 K, respectively, poleward of  $\pm 40^\circ$  latitude during local winter, and about half these values during local summer, and equatorward of these limits during all months of the year. These estimates are based upon an average SPW1 amplitude of 4.0 K at high latitudes during local winter, and about 2.0 K at other times and locations.

unknown, but appears to be a real and persistent feature of the 85–95-km height region.

A similar depiction for the semidiurnal tidal component is provided in Fig. 11. Amplitudes for the semidiurnal tide are generally of order 2–6 K for SW2 and 1–2 K for SW1 and SW3; that is, roughly half of those of the

diurnal tides depicted in Fig. 10. Moreover, potential aliasing contributions to SW1 and SW3 due to SPW1 variability are larger than for D0 and DW2, with an upper bound of 1.2 K poleward of  $\pm 40^\circ$  latitude during local winter, and about half these values during local summer, and equatorward of these limits during all months of the year. SW1 and SW3 amplitudes tend to be confined to latitudes between  $\pm 40^\circ$  latitude, whereas for SW2 large amplitudes occur at high latitudes during some seasons. This is consistent with the observation made in connection with Fig. 8, higher-order Hough modes (which tend to maximize at higher latitudes than the lower-order modes) are required to capture the latitude variations of SW2 than SW1 and SW3, which are adequately represented by a sum of the first symmetric and first antisymmetric Hough functions. The source for these higher-order modes is mode coupling due to interactions between the fundamental modes and the zonal mean wind structure (Lindzen and Hong 1974; Forbes 1982). For SW1, there are some  $\sim 1$  K amplitudes in the local winter seasons at middle to high latitudes in the Northern and Southern Hemispheres. At least in the Southern Hemisphere, this amplitude distribution is different than what one would expect on the basis of wind observations near 94 km over South Pole (Forbes et al. 1995, 1999; Portnyagin et al. 1998), which indicate maximum SW1 meridional wind amplitudes during local summer. Modeling work is apparently needed to explain these differences.

### 7. The eastward-propagating diurnal tide with zonal wavenumber $s = 3$ (DE3), and internal consistency between tidal winds and temperatures

DE3 is a prominent oscillation in the sample spectra of Fig. 3. Modeling studies (Forbes et al. 2001; Hagan and Forbes 2002) show that this oscillation is forced primarily by latent heat release due to deep tropical convection. DE3 was found to be the largest of all the nonmigrating diurnal tidal components in the tidal analysis of UARS winds at 95 km by Talaat and Lieberman (1999), Forbes et al. (2003), and Manson et al. (2004). In this section we present our results for DE3, and in addition use a methodology involving Hough mode extensions (HMEs; Lindzen et al. 1977; Forbes and Hagan 1982) to demonstrate consistency with UARS DE3 wind determinations (Forbes et al. 2003) near 95 km. As noted in the introduction, this type of exercise develops confidence in utilizing different data types together in assimilation schemes aimed at specifying the dynamical state of the MLT.

The temperature amplitude of DE3 as derived from

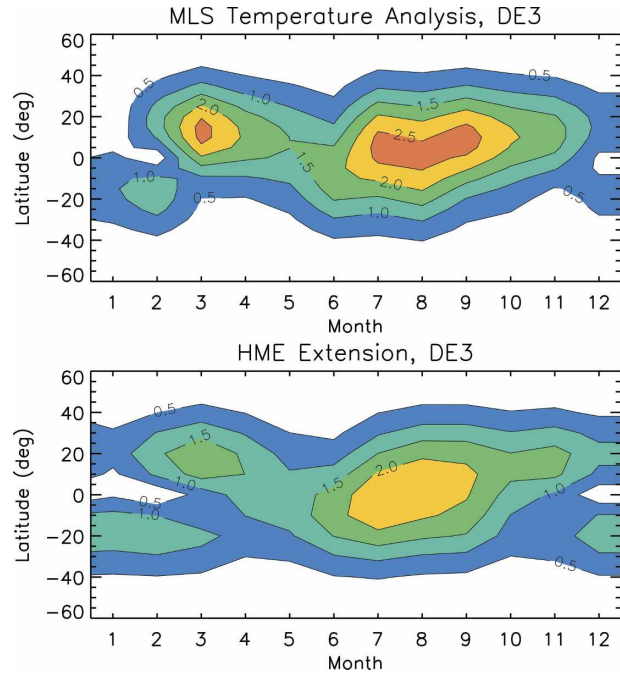


FIG. 12. Latitude vs month contours of DE3 diurnal temperature amplitudes at 86 km. (top) From present analysis of MLS temperatures at 86 km. (bottom) Derived from HME fit to DE3 eastward and northward winds at 95 km from WINDII and HRDI measurements on UARS (Forbes et al. 2003).

the MLS data at 86 km is plotted versus latitude and month in Fig. 12. At these altitudes the maximum amplitude is about 2.5–3.0 K, significantly smaller than the maximum amplitude of 8 K for DW1, but during July, DE3 is in fact stronger than DW1 at these altitudes. It is clear that during some months of the year the DE3 amplitude structure is very asymmetric with respect to the equator, whereas during Northern Hemisphere summer DE3 is predominantly symmetric with a Kelvin wave latitudinal structure. The degree of asymmetry during the various months is in fact consistent with the eastward and northward wind structures at 95 km displayed in Forbes et al. (2003). We will now examine the consistency between the temperature perturbations at 86 km and the wind perturbations at 95 km in a more quantitative way, which involves a set of basis functions called Hough mode extensions. A brief description of HMEs will now be provided, and their use in providing new information on measurements in the MLT region will be explored. Due to lack of knowledge of in situ excitation sources associated with trapped components in the DW1 and DW2 fields, and the large uncertainties in our D0 results, we will confine our attention concerning application of HMEs to the DE3. DE3 has no known sources of excitation in the mesosphere or lower thermosphere, making it a viable candidate for appli-

cation of the HME technique. In addition, the first symmetric component of DE3 has a long vertical wavelength ( $\approx 56$  km) and hence is comparatively insensitive to dissipation. As will become evident below, this is an important consideration for the application at hand.

The concept of HMEs was developed by Lindzen et al. (1977) and Forbes and Hagan (1982) in order to deal with the changes in shape of Hough modes as they encountered dissipation in an atmospheric regime above that of wave forcing. A Hough mode extension represents the global solution (pole-to-pole, 0-to-250-km altitude) to the linearized dynamical equations of the atmosphere for an oscillation of given frequency and zonal wavenumber, taking into account dissipative effects (i.e., radiative cooling, eddy and molecular diffusion of heat and momentum) above the forcing region. The HMEs are forced with a conveniently normalized heat source confined to the troposphere, and with latitude shape given by the corresponding classical Hough mode. For a given  $s$  and  $\sigma$ , an HME can be thought of as a latitude versus height table of amplitudes and phases for the velocity, temperature and density perturbation fields ( $u, w, v, T, \rho$ ) of the oscillation. The  $u, w, v, T, \rho$  perturbation fields maintain internally self-consistent relative amplitude and phase relationships for any given HME. So, if the amplitude and phase of the perturbation wind field is known for a given HME at a single latitude and height, then all the fields,  $u, w, v, T, \rho$ , are known for all latitudes and all heights.

The methodology for fitting HMEs to observational data is fully described in Forbes et al. (1994), and has also been applied in Mars atmosphere (Forbes et al. 2004a). Forbes et al. (1994) used HMEs for the migrating semidiurnal tide to simultaneously fit semidiurnal tidal winds and temperatures between 80 and 150 km, and by reconstruction arrived at a monthly climatological model of horizontal and vertical winds, temperatures and densities in this height region. In more recent work, Svoboda et al. (2005) utilize HMEs for migrating and nonmigrating diurnal tides to fit UARS tidal winds at 95 km to similarly arrive at an internally consistent global climatology of tidal temperatures, winds and densities in the 80–120-km height region. Although zonal mean winds are neglected in the computation of HMEs, this does not imply that the effects of mean winds are neglected in fitting or reconstructing tidal structures. To first order, the distortion of tidal structures due to mean winds can be viewed as mode coupling (Lindzen and Hong 1974); that is, the excitation of higher-order modes that combine together in a linear sense to approximate the distortion. In the same sense, a few HMEs can be fit to a tidal field in a way that the

weighted superposition of these HMEs reproduces the observed distortion. The methodology assumes that all of the important mean-wind effects occur below the region in which the HME fitting occurs; that is, in association with the mesospheric jets; in other words, that the 80–100-km winds are too weak to produce any significant distortion of the tidal structures. The reader is referred to Forbes et al. (1994) and Svoboda et al. (2005) for further information and details on the HME technique, its applications and limitations.

Figure 12 compares the latitude versus time evolution of DE3 temperature amplitude at 86 km from the work of Svoboda et al. (2005), and that from the present MLS analysis. The similarity between DE3 amplitudes in Fig. 12 is striking, and represents a cross-validation of the results and methodologies presented here and in Forbes et al. (2003), and indeed of the HME methodology and our understanding of tidal propagation and dissipation in general. In addition, this result lends confidence to the combined utilization of space-based temperature and wind measurements in assimilation schemes to specify the dynamical state of the upper atmosphere, at least in terms of variations about the zonal mean state are concerned.

In the interpretation of Fig. 12, there are some underlying issues that need to be addressed. In extrapolating tidal wind fields at 95 km to tidal temperature fields at 86 km, the vertical structure of the HMEs, and hence the dissipation assumed in the model, assumes importance. In the region of interest, the model includes non-LTE (local thermodynamic equilibrium) radiative cooling by  $\text{CO}_2$  as parameterized by McLandress (2002) based on the Canadian Middle Atmosphere Model (CMAM), and eddy diffusion. Molecular diffusion becomes important above 100 km. The eddy diffusion profile between 80 and 100 km is constant at  $200 \text{ m}^2 \text{ s}^{-1}$ , decreasing to smaller values outside this altitude range in a manner similar to that displayed in Forbes (1982).

Dissipation relates to the interpretation of the top two panels in Fig. 12 in the following way. The DE3 response can be decomposed into two primary Hough mode components, the first symmetric component, which is a Kelvin wave with inviscid vertical wavelength of 56 km, and the first antisymmetric component which is an inertio-gravity wave with 30 km inviscid vertical wavelength. Between the 81.4- and 97.9-km grid points in the numerical model, the HMEs corresponding to both of these waves retain their inviscid vertical wavelengths in the presence of the dissipation noted above. In addition, growth of the first symmetric HME is the same (factor of 3.3) as exponential ( $e^{z/2H}$ ) growth in the absence of dissipation, whereas that of the first anti-

symmetric mode is a factor of 2.4. This difference reflects the shorter vertical wavelength of the latter, and the fact that the time constant for dissipation is proportional to the square of the vertical wavelength. If we focus on the symmetric part of the response (i.e., the Kelvin wave response in June–October), then a larger eddy diffusion coefficient would reduce the exponential growth in the HME, and improve the agreement in Fig. 12 by making the amplitudes in the lower panel larger. However, any change in this direction would be a weak function of the eddy diffusion coefficient due to the long vertical wavelength of the Kelvin wave, and moreover, a significantly larger value of eddy diffusion coefficient is unlikely. A smaller eddy diffusion coefficient would not change the comparison between the symmetric parts of the response in Fig. 12, since the exponential growth would remain at the inviscid rate  $e^{z/2H}$ . Thus, we view this as a robust result.

The comparison in Fig. 12, particularly that part corresponding to the Kelvin wave signature in July–October, may also be relevant to the controversy surrounding discrepancies between space-based (SB) and ground-based (GB) radar measurements of winds near 95-km altitude (i.e., Burrage et al. 1996; Meek et al. 1997; Portnyagin et al. 1999; Forbes et al. 2004b) that emerged in connection with the *UARS* mission. Although there is not complete uniformity among these results, in general the zonal wind measurements from space tend to exceed those from the ground by ~60% near 95 km, with significantly better agreement between measurements below 90 km. These results pertain to both instantaneous overflight and climatological comparisons between the two datasets. Of particular relevance in the present context are the results of Forbes et al. (2004b) with regard to comparisons between GB and SB climatological diurnal tide amplitudes. They show a similar SB–GB discrepancy for the radar at Adelaide (35°S, 138°E), but much better agreement for the radar at the geographically conjugate station of Shigaraki (35°N, 136°E). Possible reasons for all of the above differences are discussed in the aforementioned papers, including differences in radar types, but the issue remains unresolved. Recall that the temperatures depicted in the lower panel of Fig. 12 are based solely on a fit of the first symmetric and first antisymmetric HMEs to DE3 diurnal wind structures at 95 km. The fact that the HME temperatures agree well with (and in fact slightly underestimate) the MLS temperature amplitudes (upper panel of Fig. 12) supports the integrity of the space-based wind measurements with respect to the diurnal tide. Of course, this assumes that the MLS temperature variations reflect those of the atmosphere, and the HMEs to embody the correct tem-

perature–wind relationship between 86 and 95 km, which depends to some degree on the assumed background temperature, density and dissipation assumed in the HME calculations. We have demonstrated that our result is robust with respect to dissipation, which is by far the issue of greatest importance. Thus, we consider our result to represent a credible and important contribution to the debate surrounding the discrepancy between GB and SB wind measurements, in addition to contributing to measurement validation in support of data-model assimilation efforts that have yet to be applied to the MLT region.

## 8. Conclusions

Analyses of temperatures measured between 25 and 86 km by the Microwave Limb Sounder (MLS) experiment on *UARS* reveal the presence of migrating (sun-synchronous) and nonmigrating solar tides. Emphasis is placed on the MLS upper altitude limit of 86 km where amplitudes are largest and aliasing effects are minimized. Our results for 86 km are as follows:

- Diurnal migrating tide (DW1) temperature amplitudes maximize near the equinoxes and between  $\pm 40^\circ$  latitude with amplitudes of order 10 K. Significant amplitudes (2–4 K) also exist at high latitudes ( $60^\circ$ – $70^\circ$ ), indicating the presence of trapped modes, possibly indicative of an in situ source of excitation (i.e., chemical heating).
- Semidiurnal migrating tide (SW2) temperature amplitudes are generally of order 2–4 K during most months over a wide range of latitudes, maximizing at 4–6 K at low latitudes during February and during the spring at  $\pm 60^\circ$  latitude.
- Diurnal nonmigrating tides D0 and DW2 exist with maxima near the equator and  $-50^\circ$  to  $-60^\circ$  latitude of order 3 K. The former feature is indicative of propagating modes, while the latter is associated with trapped components for DW2 and mainly trapped components for D0. The same nonmigrating tidal components with similar latitudinal asymmetry were found in *UARS* wind measurements at 95 km between  $\pm 40^\circ$  latitude by Forbes et al. (2003). Origins for these waves probably lie in zonally-asymmetric heat sources of unknown origin, possibly augmented by nonlinear interactions between DW1 and the stationary planetary wave with  $s = 1$  (SPW1).
- Semidiurnal nonmigrating tides SW1 and SW3 and terdiurnal nonmigrating tides TW2 and TW4 are also revealed, with amplitudes of order 1–2 K. Although relatively low in amplitude at 86 km, these waves are expected to grow to 10–12 K by the time they reach

their maxima in the lower thermosphere (~110–140 km) and thus can contribute significantly to the dynamics of this atmospheric regime (see, e.g., Angelats i Coll and Forbes 2002). These tidal components probably arise through nonlinear interactions between the migrating tides SW2 and TW3, and SPW1.

- DE3 achieves temperature amplitudes of order 3 K at low latitudes during March and July–September. This wave is probably generated by latent heat release due to deep tropical convection.
- Within the confines of dissipative tidal theory, and subject to some caveats, internal consistency is established between the MLS DE3 temperatures at 86 km and previously derived DE3 winds at 95 km. This result lends confidence to the combined use of space-based temperature and wind measurements in assimilative modeling of MLT dynamics, at least in terms of variations about the zonal mean are concerned. In addition, the integrity of space-based wind measurements demonstrated within this context may have some bearing on the debate surrounding inconsistencies sometimes noted between winds measured from the ground and space near 95 km.

### APPENDIX

#### Aliasing due to an Evolving Stationary Planetary Wave

A concern that naturally arises in space-based sampling of atmospheric structures, particularly those that are nonstationary, is that of aliasing; that is, when the energy of one sampled component leaks into another. Consider an  $s = 1$  stationary planetary wave (SPW1) whose amplitude varies with time; that is,  $A(t) \cos \lambda$  (without loss of generality the longitude of maximum is assumed at  $\lambda = 0$ ). In the satellite frame, for sampling over a complete yaw period, any temporal variability maps into local time covering 24 h:

$$A(t)|_{\text{yaw}} \cos \lambda \rightarrow A(t_{\text{LT}})|_0^{24} \cos \lambda, \quad (\text{A1})$$

which can then be Fourier-decomposed into subharmonics of a solar day:

$$\begin{aligned} A(t_{\text{LT}})|_0^{24} \cos \lambda &= \sum_{n=1}^N \cos n \Omega t_{\text{LT}} \cos \lambda \\ &= \sum_{n=1}^N \cos(n \Omega t_{\text{LT}} \pm \lambda), \end{aligned} \quad (\text{A2})$$

where  $\Omega = 2\pi \text{ day}^{-1}$  and time is in days. Transforming to canonical form for atmospheric oscillations by letting  $t_{\text{LT}} = t + \lambda/\Omega$ , we have

$$A(t)|_{\text{yaw}} \cos \lambda \rightarrow \sum_{n=1}^N \cos[n \Omega t + (n \pm 1)\lambda]. \quad (\text{A3})$$

Therefore, a time variation in SPW1, from the satellite perspective, aliases into diurnal tides ( $n = 1$ ) with zonal wavenumbers  $s = (n \pm 1) = 0, 2$ ; semidiurnal tides ( $n = 2$ ) with  $s = 1, 3$ ; terdiurnal tides ( $n = 3$ ) with  $s = 2, 4$ ; and so on. The reverse process also holds. That is, time variations in the above nonmigrating tides can alias into SPW1. However, the nonmigrating tidal amplitudes are considerably smaller in magnitude, hence the scenario (A1)–(A3) is of the greatest concern.

To gain insight into the aliasing effect, the following experiment was performed. The Mass Spectrometer and Incoherent Scatter Extended 1990 model (MSISE90; Hedin 1991), with local time variations suppressed, was identically sampled both spatially and temporally as the MLS temperature measurements. Note that the MSISE90 model used in this fashion contains only time-varying stationary planetary waves and zonal means, and no tides. The resulting data were analyzed for nonmigrating tides in a fashion identical to that described previously for the MLS temperature data. The results for  $+60^\circ\text{N}$  are shown in Fig. A1. The SPW1 amplitudes are of order 2–10 K with maximum values during local winter and spring. The other panels illustrate the derived D0, SW1, and TW2 amplitudes that arise from aliasing, which are also representative of results for DW2, SW3, and TW4, respectively. The nonmigrating tidal amplitudes are of order 0.2–0.4 K for D0 and TW2, and 0.2–1.0 K for SW1. Maxima tend to occur during periods of greatest variation in SPW1 amplitudes over a yaw cycle; that is, November, January, and April–June. As a general rule, the amplitudes of nonmigrating tides due to aliasing by an evolving SPW1 do not exceed 10% of the SPW1 amplitudes. However, we note that the mesospheric SPW1 amplitudes for MSISE90 underestimate those of MLS by at least a factor of 2 (i.e., compare the upper right-hand side panels of Fig. A1 and Fig. 5). Moreover, the SPW1 variability in the MLS data may be different than that in MSISE90. Therefore, to obtain better quantitative estimates of aliasing contributions to the nonmigrating tides, we utilize the MLS data itself to make this estimate. The method is described below.

First, it must be recognized that what is important in determining aliasing amplitudes is how well the tidal Fourier harmonics project onto the SPW1 variability over the whole span of MLS sampling. Because we are compositing multiple years of data into a single effective yaw cycle prior to analysis, year-to-year variability diminishes the coherence of the seasonal evolution of SPW1 over the fitting interval. In addition, because

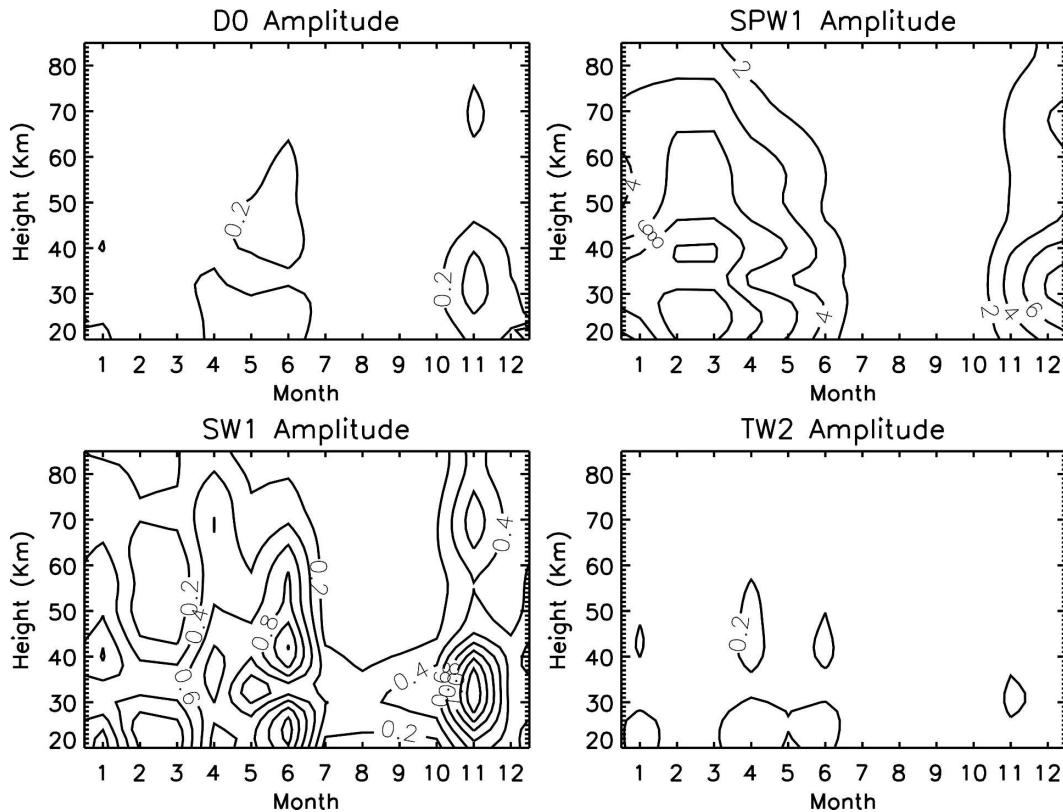


FIG. A1. Amplitudes of (top left) DW2, (top right) SPW1, (bottom left) SW1, and (bottom right) TW2 as a function of height and month at  $+60^\circ$  latitude, obtained by sampling the MSISE90 model with local time variations suppressed (i.e., no tides) according to the MLS temperature measurements during 1 Nov 1991–27 Oct 1994. The tidal components primarily reflect aliasing due to SPW1 variability over the fitting intervals. Contour spacing is 0.2 K for the tidal components, and 2.0 K for SPW1.

MLS views  $90^\circ$  from the orbital plane, the local times at the tangent point differ by  $\sim 3$  h before and after a yaw. This irregular sampling helps to reduce the aliasing. The contributions of both of these effects reduce the potential for aliasing that would exist during a single season.

One cannot determine the SPW1 variability in the MLS data over time scales less than a 36-day yaw cycle, because at these time scales the SPW1 variations cannot be separated from the nonmigrating tides. However, following on the example provided above and illustrated in Figure A1, we now propose a method for arriving at quantitative aliasing estimates. The method is based on the following assumptions: (i) tidal amplitudes at 20–40 km in the stratosphere are negligibly small, and (ii) variability of the SPW1 in the rest of the domain follows that in the stratosphere. Note that (i) implies that any tidal amplitudes recovered in the MLS analysis between 20–40 km are due to aliasing by SPW1 variability. Comparison of the nonmigrating tidal amplitudes with those of the SPW1 in the stratosphere

provides a measure of how well the SPW1 variability projects onto the nonmigrating tidal components over the 3-yr climatology of the MLS temperature measurements. Assumption (ii) implies that this amplitude ratio extends throughout the mesosphere, and can be used to estimate the aliasing contributions to nonmigrating tides provided we know the magnitude of SPW1 at those levels. This is equivalent to saying that the SPW1 variability projects onto the nonmigrating tides with the same efficiency everywhere. This is of course not strictly true, but an assumption of this nature is required to arrive at a quantitative estimate. Furthermore, since some fraction of the observed nonmigrating tidal signals in the stratosphere may be due to SPW1 interactions with migrating tidal components (whose amplitudes are nonnegligible in the regions of interest), we consider our aliasing estimates to represent an upper bound. Therefore, to summarize, a tidal amplitude in the mesosphere due to aliasing by SPW1 variability is assumed to be bounded [following assumption (ii) above], as follows:

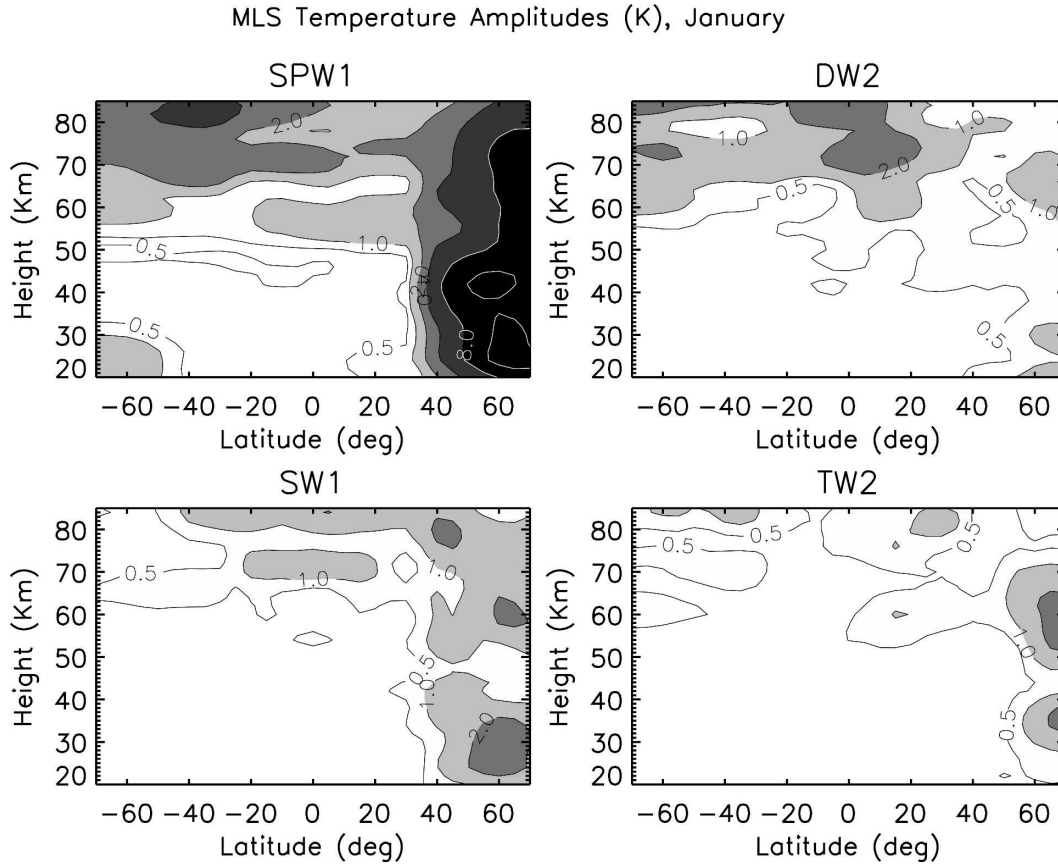


FIG. A2. MLS temperature amplitudes (K) as a function of height and latitude during January for (top left) SPW1, (top right) DW2, (bottom left) SW1, and (bottom right) TW2. Contours are at 0.5, 1.0, 2.0, 4.0, 8.0, and 12.0 K for all panels.

$$|\text{Tide}_{\text{mesosphere}}|_{\text{alias}} \leq \left[ \frac{|\text{SPW1}_{\text{mesosphere}}|}{|\text{SPW1}_{\text{stratosphere}}|} \frac{|\text{Tide}_{\text{stratosphere}}|}{|\text{SPW1}_{\text{stratosphere}}|} \right]_{\text{observed}}, \quad (\text{A4})$$

where  $|\text{Tide}_{\text{stratosphere}}|_{\text{alias}} = |\text{Tide}_{\text{stratosphere}}|_{\text{observed}}$  according to assumption (i) above.

An example of how these aliasing estimates were obtained is now provided. Refer to Fig. A2, where we provide height versus latitude contours of SPW1, DW2, SW1, and TW2 amplitudes for the month of January. Note the equatorward and interhemispheric penetration of SPW1, similar to that found in UARS wind measurements (Forbes et al. 2002) and in numerical simulations (Pogoreltsev and Sukhanova 1993). Significant amplitudes are even found in the Southern Hemisphere at 86 km. Average SPW1 amplitudes are of order 8 K in the high-latitude Northern Hemisphere winter stratosphere. With respect to SPW1, average nonmigrating tidal amplitude ratios in the same regime

are of order 7% for DW2, 20% for SW1, and 7% for TW2. Similar results are obtained for D0, SW3, and TW4. (Recall from section 2 that January is one of those months where the potential for aliasing is suspected to be particularly high, since the 15th of the month falls in the gap between yaw cycles, and about half the local times binned together originate in the previous and following yaw cycles.) We now assume that the same proportionality applies throughout the domain, and obtain aliasing estimates at (for example) 86 km of order 0.07–0.28 K for DW2 and TW2, and of order 0.20–0.80 K for SW1. This is the method used to provide upper bounds on aliasing contributions to nonmigrating tidal components throughout the text and in the figure captions.

The above method was applied to all months, and the following average values were found: 13% for D0, 6% for DW2, 30% for SW1, 26% for SW3, 7% for TW2, and 11% for TW4. In some cases these average values are used to provide rough upper limits on the aliasing contributions due to SPW1 variability (cf. Figs. 10, 11).

It is interesting to note the significantly larger aliasing estimates for the semidiurnal nonmigrating tides, similar to the results illustrated in Fig. A1 using the MSISE90 model.

*Acknowledgments.* The authors thank Ms. Xiaoli Zhang for her assistance in data processing and figure preparation. This work was supported under Grant FA9550-05-1-0071 from the Air Force Office of Scientific Research to the University of Colorado.

#### REFERENCES

- Angelats i Coll, M., and J. M. Forbes, 2002: Nonlinear interactions in the upper atmosphere: The  $s = 1$  and  $s = 3$  nonmigrating semidiurnal tides. *J. Geophys. Res.*, **107**, 1157, doi:10.1029/2001JA900179.
- Burrage, M. D., and Coauthors, 1996: Validation of mesosphere and lower thermosphere winds from the High Resolution Doppler Imager on UARS. *J. Geophys. Res.*, **101**, 10 365–10 392.
- Chapman, S., and R. S. Lindzen, 1970: *Atmospheric Tides: Thermal and Gravitational*. Gordon and Breach, 200 pp.
- Conrath, B. J., 1976: Influence of planetary-scale topography on the diurnal thermal tide during the 1971 Martian dust storm. *J. Atmos. Sci.*, **33**, 2430–2439.
- Ekanayake, E. M. P., T. Aso, and S. Miyahara, 1997: Background wind effect on propagation of nonmigrating diurnal tides in the middle atmosphere. *J. Atmos. Solar-Terr. Phys.*, **59**, 401–429.
- Forbes, J. M., 1982: Atmospheric tides 2. The solar and lunar semidiurnal components. *J. Geophys. Res.*, **87**, 5241–5252.
- , and M. E. Hagan, 1982: Thermospheric extensions of the classical expansion functions for semidiurnal tides. *J. Geophys. Res.*, **87**, 5253–5259.
- , and F. Vial, 1989: Monthly simulations of the solar semidiurnal tide in the mesosphere and lower thermosphere. *J. Atmos. Terr. Phys.*, **51**, 649–662.
- , and —, 1991: Semidiurnal tidal climatology of the E Region. *J. Geophys. Res.*, **96**, 1147–1157.
- , and Coauthors, 1994: Semidiurnal tide in the 80–150 km region: An assimilative data analysis. *J. Atmos. Terr. Phys.*, **56**, 1237–1250.
- , N. A. Makarov, and Yu. I. Portnyagin, 1995: First results from the meteor radar at South Pole: A large 12-hour oscillation with zonal wavenumber one. *Geophys. Res. Lett.*, **22**, 3247–3250.
- , M. E. Hagan, X. Zhang, and K. Hamilton, 1997a: Upper atmosphere tidal oscillations due to latent heat release in the tropical troposphere. *Ann. Geophys.*, **15**, 1165–1175.
- , M. Kilpatrick, D. Fritts, A. Manson, and R. Vincent, 1997b: Zonal mean and tidal dynamics from space: An examination of aliasing and sampling issues. *Ann. Geophys.*, **15**, 1158–1164.
- , Yu. I. Portnyagin, N. A. Makarov, S. E. Palo, E. G. Merzlyakov, and X. Zhang, 1999: Dynamics of the lower thermosphere over South Pole from meteor radar wind measurements. *Earth Planet. Space*, **51**, 611–620.
- , X. Zhang, and M. E. Hagan, 2001: Simulations of diurnal tides due to tropospheric heating from the NCEP/NCAR reanalysis Project. *Geophys. Res. Lett.*, **28**, 3851–3854.
- , —, W. Ward, and E. Talaat, 2002: Climatological features of stationary planetary waves in the stratosphere, mesosphere and lower thermosphere between  $\pm 40^\circ$  latitude. *J. Geophys. Res.*, **107**, 4322, doi:10.1029/2001JD001232.
- , —, —, and —, 2003: Nonmigrating diurnal tides in the thermosphere. *J. Geophys. Res.*, **108**, 1033, doi:10.1029/2002JA009262.
- , —, M. Angelats i Coll, and G. M. Keating, 2004a: Nonmigrating tides in the thermosphere of Mars: A quasi-empirical description. *Adv. Space Res.*, **34**, 1690–1695.
- , Yu. I. Portnyagin, W. Skinner, R. Vincent, T. Solovjova, E. Merzlyakov, T. Nakamura, and S. Palo, 2004b: Climatological lower thermosphere winds as seen by ground-based and space-based instruments. *Ann. Geophys.*, **22**, 1931–1945.
- Grieger, N., E. M. Volodin, G. Schmitz, P. Hoffmann, A. H. Manson, D. C. Fritts, K. Igarashi, and W. Singer, 2002: General Circulation Model results on migrating and nonmigrating tides in the mesosphere and lower thermosphere. Part 1: Comparison with observations. *J. Atmos. Solar-Terr. Phys.*, **64**, 897–911.
- , G. Schmitz, and U. Achatz, 2004: The dependence of nonmigrating diurnal tide in the mesosphere and lower thermosphere on stationary planetary waves. *J. Atmos. Solar-Terr. Phys.*, **66**, 733–754.
- Hagan, M. E., and R. G. Roble, 2001: Modeling diurnal tidal variability with the NCAR TIME-GCM. *J. Geophys. Res.*, **106**, 24 869–24 882.
- , and J. M. Forbes, 2002: Migrating and nonmigrating diurnal tides in the middle and upper atmosphere excited by tropospheric latent heat release. *J. Geophys. Res.*, **107**, 4754, doi:10.1029/2001JD001236.
- , and —, 2003: Migrating and nonmigrating semidiurnal tides in the middle and upper atmosphere excited by tropospheric latent heat release. *J. Geophys. Res.*, **108**, 1062, doi:10.1029/2002JA009466.
- , J. L. Chang, and S. K. Avery, 1997a: GSWM estimates of nonmigrating tidal effects. *J. Geophys. Res.*, **102**, 16 439–16 452.
- , C. McLandress, and J. M. Forbes, 1997b: Diurnal tidal variability in the upper mesosphere and lower thermosphere. *Ann. Geophys.*, **15**, 1176–1186.
- , M. D. Burrage, J. M. Forbes, J. Hackney, W. J. Randel, and X. Zhang, 1999: GSWM-98: Results for migrating solar tides. *J. Geophys. Res.*, **104**, 6813–6827.
- Hedin, A. E., 1991: Extension of the MSIS thermosphere model into the middle and lower atmosphere. *J. Geophys. Res.*, **96**, 1159–1172.
- Hendon, H. H., and K. Woodberry, 1993: The diurnal cycle of tropical convection. *J. Geophys. Res.*, **98**, 16 623–16 637.
- Huang, F. T., and C. A. Reber, 2004: Nonmigrating semidiurnal and diurnal tides at 95 km based on wind measurements from the High Resolution Doppler Imager on UARS. *J. Geophys. Res.*, **109**, D10110, doi:10.1029/2003JD004442.
- Lieberman, R. S., 1991: Nonmigrating diurnal tides in the equatorial middle atmosphere. *J. Atmos. Sci.*, **48**, 1112–1123.
- , J. Oberheide, M. E. Hagan, E. E. Remsberg, and L. L. Gordley, 2004: Variability of diurnal tides and planetary waves during November 1978–May 1979. *J. Atmos. Solar-Terr. Phys.*, **66**, doi:10.1016/j.jastp.2004.01.006.
- Lindzen, R. S., 1976: A modal decomposition of the semidiurnal tide in the lower thermosphere. *J. Geophys. Res.*, **81**, 2923–2926.

- , and S.-S. Hong, 1974: Effects of mean winds and horizontal temperature gradients on solar and lunar semidiurnal tides in the atmosphere. *J. Atmos. Sci.*, **31**, 1421–1446.
- , —, and J. M. Forbes, 1977: Semidiurnal Hough mode extensions into the thermosphere and their application. Memo. Rep. 3442, Naval Research Laboratory, Washington, DC, 65 pp.
- Manson, A. H., Y. Luo, and C. Meek, 2002: Global distributions of diurnal and semi-diurnal tides: Observations from HRDI-UARS of the MLT Region. *Ann. Geophys.*, **20**, 1877–1890.
- , C. Meek, M. E. Hagan, X. Zhang, and Y. Luo, 2004: Global distributions of diurnal and semidiurnal tides: Observations from HRDI-UARS of the MLT region and comparisons with GSWM-02 (migrating, nonmigrating components). *Ann. Geophys.*, **22**, 1529–1548.
- McLandress, C., 2002: The seasonal variation of the propagating diurnal tide in the mesosphere and lower thermosphere. Part II: The role of tidal heating and zonal mean winds. *J. Atmos. Sci.*, **59**, 907–922.
- , and W. E. Ward, 1994: Tidal/gravity wave interactions and their influence on the large scale dynamics of the middle atmosphere: Model results. *J. Geophys. Res.*, **99**, 8139–8156.
- Meek, C. E., A. H. Manson, M. D. Burrage, G. Garbe, and L. L. Cogger, 1997: Comparisons between Canadian Prairie MF Radars, FPI (green and OH lines) and UARS HRDI systems. *Ann. Geophys.*, **15**, 1099–1110.
- Miyahara, S., Y. Miyoshi, and K. Yamashita, 1999: Variations of migrating and nonmigrating tides simulated by the middle atmosphere circulation model at Kyushu University. *Adv. Space Res.*, **24**, 1549–1558.
- Mlynczak, M. G., and S. Solomon, 1993: A detailed evaluation of the heating efficiency in the middle atmosphere. *J. Geophys. Res.*, **98**, 10 517–10 541.
- Oberheide, J., and O. A. Gusev, 2002: Observation of migrating and nonmigrating diurnal tides in the equatorial lower thermosphere. *Geophys. Res. Lett.*, **29**, 2167, doi:10.1029/2002GL016213.
- , M. E. Hagan, R. G. Roble, and D. Offermann, 2002: Sources of nonmigrating tides in the tropical middle atmosphere. *J. Geophys. Res.*, **107**, 4567, doi:10.1029/2002JD002220.
- Pogoreltsev, A. I., and S. A. Sukhanova, 1993: Simulation of the global structure of stationary planetary waves in the mesosphere and lower thermosphere. *J. Atmos. Terr. Phys.*, **55**, 33–40.
- Portnyagin, Yu. I., J. M. Forbes, N. A. Makarov, E. G. Merzlyakov, and S. Palo, 1998: The summertime 12-hour wind oscillation with zonal wavenumber  $s = 1$  in the lower thermosphere over South Pole. *Ann. Geophys.*, **16**, 828–837.
- , T. V. Solovjova, and D. Y. Wang, 1999: Some results of comparison between the lower thermosphere zonal winds as seen by the ground-based radars and WINDII on UARS. *Earth Planet. Space*, **51**, 701–709.
- Smith, A. K., 2000: Structure of the terdiurnal tide at 95 km. *Geophys. Res. Lett.*, **27**, 177–200.
- , and D. A. Ortland, 2001: Modeling and analysis of the structure and generation of the terdiurnal tide. *J. Atmos. Sci.*, **58**, 3116–3134.
- , D. R. Marsh, and A. C. Szymczak, 2003: Interaction of chemical heating and the diurnal tide in the mesosphere. *J. Geophys. Res.*, **108**, 4164, doi:10.1029/2002JD002664.
- Svoboda, A. A., J. M. Forbes, and S. Miyahara, 2005: A space-based climatology of MLT winds, temperatures and densities from UARS wind measurements. *J. Atmos. Solar-Terr. Phys.*, **67**, 1533–1543.
- Talaat, E. R., and R. S. Lieberman, 1999: Nonmigrating diurnal tides in mesospheric and lower thermospheric winds and temperatures. *J. Atmos. Sci.*, **56**, 4073–4087.
- Teitelbaum, H., and F. Vial, 1991: On tidal variability by nonlinear interaction with planetary waves. *J. Geophys. Res.*, **96**, 14 169–14 178.
- Tokioka, T., and I. Yagai, 1987: Atmospheric tides appearing in a global atmospheric general circulation model. *J. Meteor. Soc. Japan*, **65**, 423–437.
- Williams, C. R., and S. K. Avery, 1996: Diurnal nonmigrating tidal oscillations forced by deep convective clouds. *J. Geophys. Res.*, **101**, 4079–4091.
- Wu, D. L., and Coauthors, 2003: Mesospheric temperature from UARS MLS: Retrieval and validation. *J. Atmos. Solar-Terr. Phys.*, **65**, 245–267.
- Yagai, I., 1989: Nonmigrating thermal tides detected in data analysis and a general circulation model simulation. *J. Geophys. Res.*, **94**, 6341–6356.
- Yamashita, K., S. Miyahara, Y. Miyoshi, K. Kawano, and J. Ni-nomiya, 2002: Seasonal variation of non-migrating semidiurnal tide in the polar MLT region in a general circulation model. *J. Atmos. Solar-Terr. Phys.*, **64**, 1083–1094.
- Zurek, R. W., 1976: Diurnal tide in the Martian atmosphere. *J. Atmos. Sci.*, **33**, 321–337.